Supplementary Information

EPR-Derived Structure of a Paramagnetic Intermediate Generated by Biotin Synthase BioB

Lizhi Tao[1], Troy A. Stich[1], Corey J. Fugate[2], Joseph T. Jarrett[2] and R. David Britt[1]*

[1]Department of Chemistry, University of California, Davis, California 95616, United States

[2]Department of Chemistry, University of Hawaii at Manoa, Honolulu, Hawaii 96822, United States

*Corresponding Author: *rdbritt@ucdavis.edu*

Table of Contents

Supplementary Materials and Methods

1.1 Purification of biotin biosynthetic enzymes. Expression and purification of biotin biosynthetic enzymes including BioW, BioF, BioA and BioD were performed as described in details in reference (1). Briefly, BioW, BioF, BioA or BioD were overexpressed in *E. coli* strain BL21(DE3)pLysS with the corresponding plasmids which harbor the *B. sphaericus bioW*, and *E. coli bioF*, *bioA* or *bioD* genes, respectively. Cells were grown in Luria-Bertani (LB) broth containing appropriate antibiotics (25 mg/L kanamycin for BioW and BioA, 50 mg/L ampicillin for BioF and BioD) at 37 °C to an $O.D._{600} \approx 1.0$, and then 0.5 mM isopropyl β-D-1-thiogalactopyranoside (IPTG) was added to induce the expression. After around 3 h, cells were harvested by centrifugation, flash frozen in liquid nitrogen and stored at −80 °C.

For purifying BioW enzyme,[2] the cell pellet was resuspended in buffer A (20 mM Tris-HCl, 50 mM NaCl, pH = 8.0) and lysed by sonication. Cell debris was removed by centrifugation and the supernatant was loaded onto a DEAE fast-flow sepharose anion exchange column (2 x 12 cm) pre-equilibrated with buffer A. The column was then washed with 200 mL buffer A and eluted with a 300 mL linear gradient up to 1 M NaCl. Fractions containing BioW (~28 kDa) were verified via sodium dodecyl sulfate polyacrylamide gel electrophoresis (SDS-PAGE, Bio-Rad) and were pooled and desalted using Bio-Gel P2 size-exclusion column (2 x 20 cm, BioRad). The protein solution was further loaded onto a Reactive Red-Agarose column (1 x 4 cm) equilibrated with buffer A. The column was washed with 50 mL buffer A followed by 20 mM Tris-HCl, 2 M NaCl, pH = 8.0. The BioW containing fractions were collected and desalted using Bio-Gel P2 column into a buffer of 50 mM Tris-HCl, pH = 8.0.

For purifying BioA enzyme, the cell pellet was resuspended in HEB buffer (50 mM HEPES, 0.1 mM EDTA, 10 mM β-mercaptoethanol, pH = 8.0) and lysed by sonication. Cell debris was removed by centrifugation and the supernatant was diluted to 6 mg/mL (total protein concentration) using HEB buffer. The diluted supernatant was supplemented with 2 mM (final concentration) pyridoxal phosphate (PLP) and streptomycin sulfate. The supernatant was then clarified by heat-denaturation at 55 °C for 15 min, and then cooled to 10 °C in an ice bath. The precipitations were removed by centrifugation and the supernatant was adjusted to pH = 5.0 with acetic acid and incubated on ice for 20 min. The supernatant was further adjusted to pH = 7.0 with sodium hydroxide and incubated on ice overnight, followed by centrifugation to remove the

precipitations. Then the supernatant was loaded onto a Q sepharose column (2 x 12 cm, Sigma) equilibrated with buffer A. The column was washed with 200 mL buffer A followed with a 600 mL linear gradient up to 1 M NaCl. Fractions containing BioA (~47 kDa) were verified via SDS-PAGE as well as the UV/visible spectrum of the PLP cofactor. The protein was further desalted using Bio-Gel P2 column into the buffer of 50 mM Tris-HCl, pH = 8.0.

BioF and BioD enzymes share the same purification protocol by using Ni-NTA affinity chromatography. The corresponding cell pellet was resuspended in buffer B (50 mM Bis-Tris propane, 0.5 M NaCl, 10% glycerol, pH = 7.5), lysed by sonication and the cell debris was removed by centrifugation. The supernatant was loaded onto a Ni-NTA agarose column and washed with buffer B. The protein was eluted by using buffer B supplemented with 300 mM imidazole and verified via SDS-PAGE (BioF: ~41 kDa; BioD: ~24 kDa). To remove the imidazole in the buffer, the final protein sample was desalted using Bio-Gel P2 column into a buffer of 50 mM Bis-Tris propane, 10% glycerol, pH = 7.5.

1.2 Biosynthesis of isotopically-labeled dethiobiotin. As illustrated in Figure 1, the synthesis of dethiobiotin (DTB) requires a two-step process using four biotin biosynthetic enzymes, BioW from *B. sphaericus* and BioF, BioA and BioD from *E. coli* (*vide supra*). As described in details in reference (1), the first step is to yield and purify the pimeloyl coenzyme A (Pim-CoA). A reaction was initiated by adding 1 mg BioW[2] into a mixture containing 50 mM pimelic acid, 50 mM adenosine 5'-triphosphate (ATP), and 12 mM coenzyme A in a buffer of 50 mM Tris-HCl, 10 mM $MgCl_2$, 200 mM NaCl, pH = 8.0. The reaction mixture was incubated at 37 °C for 1 h and was then quenched by adding 400 mM sodium acetate, pH = 4.5. The quenched reaction mixture was incubated on ice for >10 min before centrifugation to remove the precipitations. The clarified solution was loaded onto a Waters Atlantis dC18 reversed-phase HPLC column (10 x 150 mm, 10 μm) equilibrated with 2% acetonitrile/H_2O (0.1% formic acid) at a flow rate of 4 mL/min. The Pim-CoA was eluted by using a linear gradient of 2 – 30% acetonitrile over 9 min and was determined by UV absorbance at 230 nm. Fractions containing Pim-CoA were pooled and lyophilized. The concentration of Pim-CoA was determined via the extinction coefficient of absorbance at 230 nm ($\varepsilon_{230} = 4500\ M^{-1}\cdot cm^{-1}$).

The second step utilized the purified BioF, BioA and BioD to synthesize the desired product, DTB, by using Pim-CoA, L-alanine along with other substrates. The reaction was initiated by adding BioF, BioA and BioD (1 mg each) to a mixture containing 10 mM $NaHCO_3$, 20 mM *S*-adenosyl-L-methionine (SAM), 20 mM ATP, 8 mM L-alanine, and 8 mM Pim-CoA in a buffer of 50 mM Bis-tris propane, 10 mM $MgCl_2$, 10% glycerol, pH = 7.5. The reaction mixture was incubated at room temperature for 24 h and was then quenched by adding 400 mM sodium acetate, pH = 4.5. The quenched reaction mixture was incubated on ice for >10 min before centrifugation to remove the precipitations. The clarified solution was loaded onto a C18 solid phase extraction column (100 mg, Alltech) equilibrated with 0.1% formic acid. The flow-through was further loaded onto a Waters Atlantis dC18 reversed-phase HPLC column (10 x 150 mm, 10 μm) equilibrated with 2% acetonitrile/H_2O (10 mM HCl) at a flow rate of 4 mL/min. DTB was eluted by using a linear gradient of 18 – 25% acetonitrile over 9 min and determined via the absorbance at 210 nm ($\varepsilon_{210\ nm}$ = 870 $M^{-1}\cdot cm^{-1}$). Fractions containing DTB were pooled and lyophilized. The concentration of DTB was determined by HPLC employing commercial DTB as a standard. All illustrated in Figure 1, for specific isotopically-labeled DTB, 3-^{13}C-L-alanine, 2-^{13}C-L-alanine, ^{15}N-L-alanine and $NaH^{13}CO_3$ was used for incorporating ^{13}C9, ^{13}C8, ^{15}N1 and ^{13}C10-DTB, respectively. For ^{2}H7-DTB, the reaction was performed in D_2O. Incorporation of the isotopes were confirmed LCMS (not shown) and by NMR spectroscopy as shown in Figure S22-S26.

1.3 Purification of biotin synthase with ^{57}Fe-labeled [2Fe−2S] cluster. Biotin synthase (BioB) with a His_6-tag was expressed as previously described.[3-4] Briefly, BioB was overexpressed in *E. coli* strain BL21(DE3)pLysS with the corresponding plasmid which harbors the gene *bioB* with an N-terminal hexahistidine tag. Cells were grown in minimal M9 medium[5] supplemented with 10 μM $^{57}FeCl_3$, 0.4% glucose, 0.4% casamino acids, antibiotics (25 mg/L chloramphenicol and 50 mg/L ampicillin) and trace elements[6] at 37 °C with vigorous shaking for 5 h. Then 0.5 mM IPTG was added to induce the expression at 25 °C. After around 4 h, cells were harvested by centrifugation, flash frozen in liquid nitrogen and stored at −80 °C. (Note: For expressing BioB containing natural abundance [2Fe−2S] cluster, the protocol is same as the procedure described above except that cells were grown in LB broth supplemented with 50 μM $FeCl_3$, 25 mg/L chloramphenicol and 50 mg/L ampicillin.)

For purifying BioB enzyme, the same protocol as purifying BioF and BioD (*vide supra*) was used by employing Ni-NTA affinity chromatography column, except that a buffer of 50 mM Tris-HCl, 0.5 M NaCl, pH = 8.0 was used instead of buffer B. The final protein was verified by SDS-PAGE and was concentrated to ~500 μM and stored in a buffer of 25 mM Tris-HCl, 25 mM NaCl, pH = 8.0. The concentration of BioB was determined via the extinction coefficient at 452 nm ($\varepsilon_{452\ nm}$ = 8400 $M^{-1}\cdot cm^{-1}$) and confirmed by the Bradford assay using bovine serum albumin as a standard.[3] Through this stage, all the expression and purification procedures were performed under aerobic conditions. The protein was then flash frozen in liquid nitrogen and stored at −80 °C.

1.4 Purification of biotin synthase with (guanidino-$^{15}N_2$)-arginine. BioB with (guanidino-$^{15}N_2$)-arginine was expressed as previously described by using *E.coli* BL21(DE3) Δ*arg*H strain.[1, 7] Cells were grown in a modified M9 medium[8] supplemented with 50 μM ferric citrate and (guanidino-$^{15}N_2$)-arginine (Cambridge Isotope Laboratories) at 37 °C to an $O.D._{600} \approx 1.0$. Then 0.5 mM IPTG was added to induce the expression at 25 °C. After around 3 h, cells were harvested by centrifugation, flash frozen in liquid nitrogen and stored at −80 °C. The labeled protein was purified and reconstituted following the same protocol as described above for the BioB with ^{57}Fe-labeled [2Fe−2S] cluster or in reference (3). The isotope incorporation of guanidino-$^{15}N_2$ of Arg260 was verified by matrix-assisted laser desorption/ionization (MALDI) mass spectrometry of peptides derived from a tryptic digestion, *see* reference (1).

2. Supplementary Text

2.1 Direct evidences of Arg260 coordinated to ferrous site. In this work, we provide direct evidence to support that Arg260 coordinates to the ferrous site in the paramagnetic intermediate. Firstly, as shown in Figure S4, for ^{15}N VMT-Mims ENDOR experiment, as t_{mix} is increased from 1 μs to 100 μs, a notable decrease in the intensity of the low RF frequency peak (α electron spin manifold) of $^{15}N_b$ is observed, indicating a positive sign of $^{15}N_b$ hyperfine coupling. For $^{15}N_a$, as only ENDOR signal from one electron spin manifold of is detected, the same analysis as $^{15}N_b$ is not applicable. However, we do observe that as increasing t_{mix} from 1 μs to 100 μs, the intensity of the high RF frequency peak of $^{15}N_a$ persists in a manner similar to that of the high RF frequency peak of $^{15}N_b$, rather than the low RF frequency peak of $^{15}N_b$ which would vanish, suggesting that $^{15}N_a$ has the same positive sign of hyperfine as $^{15}N_b$. The third ^{15}N (labeled as green, Figure S4, 3E & 3F) shown opposite asymmetric pattern suggests its negative hyperfine coupling. The same positive signs of hyperfine couplings for $^{15}N_a$ and $^{15}N_b$ confirm their same origins from the guanidino group of Arg260, while the negative hyperfine coupling for the third ^{15}N could source from the remote Arg95. As the nuclear magneton of ^{15}N is negative, the corresponding spin density on $^{15}N_a$ and $^{15}N_b$ is negative by using eq. 1 in the main text, suggesting that the guanidino group has negative spin density which is reasonably delocalized from the ferrous site (β electron spin). DFT models further support that Arg260 coordinates to the ferrous site, as the models with guanidino group coordinated to the ferric site (Figure S19) fail to yield reasonable spin distribution over the intermediate molecule. In addition, we were able to extract three sets of cysteine beta-protons with axial hyperfine couplings (*see* next section 2.2), which means there are more than one cysteine coordinated to the ferric site,[9-11] as beta-protons of cysteine coordinated to the ferrous site usually yield rhombic hyperfine coupling tensors.[9-11] Therefore, there are two cysteines coordinated to the ferric site, leaving the Arg260 as the ligand to the ferrous site.

2.2 Analysis of beta-protons. Hyperfine couplings of the beta-protons in the paramagnetic intermediate were analyzed by using ^{1}H-HYSCORE and Dikanov's analysis method based on the contour lineshape of HYSCORE spectra, which has been described in details in references (10-11). Briefly, for a nuclear spin with $I = 1/2$ coupled to an electron spin with $S =$

1/2, the contour lineshape (the ridge forming each cross-peak on a contour plot of HYSCORE spectra) of an axial hyperfine coupling is described by the following equation:

$$\nu_\alpha^2 = Q_\alpha \nu_\beta^2 + G_\alpha \qquad \text{(eq. S1)}$$

where $Q_\alpha = \frac{T + 2a_{iso} \mp 4\nu_N}{T + 2a_{iso} \pm 4\nu_N}$, $G_\alpha = \pm \frac{2\nu_N(4\nu_N^2 - a_{iso}^2 + 2T^2 - a_{iso}T)}{T + 2a_{iso} \pm 4\nu_N}$, ν_N is the nuclear Larmor frequency (14.82 MHz for ^{1}H at 348.0 mT was used in this work). When we plot the HYSCORE spectra as ν_α^2 versus ν_β^2 (Figure S6b), the contour line shape will be transformed into a straight line with the slope and intercept as Q_α and G_α, respectively. Then we can extract the corresponding values of a_{iso} and T ($a_{iso} > 0$ and $T > 0$ for beta-protons of cysteines coordinated to the ferric site of reduced $[2Fe{-}2S]^+$ cluster[9-11])

In order to compare the data of HYSCORE spectra recorded at different magnetic fields, the cross-peak frequencies (ν_α, ν_β) need to be normalized to a certain nuclear Larmor frequency ν_N (14.82 MHz for ^{1}H at 348.0 mT was used) through the following equation:

$$\nu_{\alpha(\beta)}^2 = (\nu_N \pm A/2) + B^2/4 \qquad \text{(eq. S2)}$$

where $A = \frac{\nu_\alpha^2 - \nu_\beta^2}{2\nu_N'}$, $B^2 = 2[\nu_\alpha^2 + \nu_\beta^2 - 2\nu_N'^2 - \frac{(\nu_\alpha^2 - \nu_\beta^2)}{8\nu_N'}]$, ν_N = 14.82 MHz, and ν_N' is the nuclear Larmor frequency at the magnetic field with each spectrum recorded. In this way, we can analysis the field-dependent ^{1}H-HYSCORE spectra. Around 20 – 30 data points (ν_α, ν_β) were taken along the uppermost contour for each ridge in each HYSCORE spectrum at the corresponding magnetic field (Figure S6d). Then the sets of frequencies (ν_α, ν_β) from varying magnetic fields were normalized to 14.82 MHz via eq. S2, and were plotted as ν_α^2 versus ν_β^2. In this representation, all data points will fall along several straight lines, i.e., three lines in this work, as shown in Figure S7, suggesting that three sets of beta-protons are extracted. Further by using eq. S1 and the slopes and intercepts of three straight lines, we can compute three sets of axial hyperfine coupling tensors, as given in Figure S6b. As beta-protons of cysteines coordinated to the ferrous site yield more rhombic HFI tensors,[9-11] the extracted axial HFI tensors are reasonably from the beta-protons of cysteines coordinated to the ferric site with $a_{iso} > 0$ and $T > 0$. Therefore, the corresponding hyperfine coupling values for ^{1}H1, ^{1}H2 and ^{1}H3 are given in Figure S7b and are labeled in red, green and blue, respectively.

2.3 ^{2}H7 orientation-selected ENDOR spectra. The orientation-selected ^{2}H7 Mims-ENDOR spectra are shown in Figure 6B and S12, in which at g_3 = 1.847 we were able to observe a four-line pattern comprised of two sets of splitting: one set arises from the hyperfine splitting A (~0.09 MHz); the other set arises from the quadrupole splitting, $3P$ (~0.20 MHz, < $3P_{max}$ = $3e^2Qq/2h$). When spectrum was recorded at g_2 = 1.941, we observed a three-line pattern which can be formed only under the condition that the hyperfine splitting A is comparable to the quadrupole splitting $3P$ (~0.10 MHz). These patterns at g_2 and g_3 can be well simulated with A(^{2}H7) = [0.03, 0.03, 0.09] MHz, P(^{2}H7) = [-0.02, -0.08, 0.10] MHz and Euler angle = [0, 150, 0]°. However, as this intermediate sample with ^{2}H7 incorporated was generated by using ^{2}H7-DTB and BioB with (guanidino-$^{15}N_2$)-arginine, there is signal arising from the strong coupling $^{15}N_a$ of Arg260 around the ^{2}H larmor frequency at g = 1.990, as shown in Figure S12. Therefore, it is difficult to distinguish the signal from ^{2}H7 at this magnetic field.

2.4 The *g*-tensor of two components in the paramagnetic intermediate. Consistent with our early studies,[1, 12] the EPR spectra of the generated paramagnetic intermediate in this work also contain two components with g_3 values of 1.881 and 1.847, respectively, as shown in Figure 2 and Figure S20. We previously reported that the X-band EPR spectrum can be simulated by two models:[12] model 1 contains a major component (64%) with g-values = [1.995, 1.941, 1.846] and a minor component (36%) with g-values = [2.008, 1.960, 1.879]; model 2 contains a major component (74%) with g-values = [2.004, 1.953, 1.847] and a minor component (26%) with g-values = [1.991, 1.938 1.880]. Now combining both X-band CW (Figure 2A) and Q-band electron spin-echo detected field swept absorption spectra (Figure 2B), we update the g-tensors of these two components. As shown in Figure S20, we have employed two models to fit the spectra: model 1 contains a major component (64%) with g-values = [1.993, 1.941, 1.847] and a minor component (36%) with g-values = [2.005, 1.960, 1.881]; model 2 contains a major component (67%) with g-values = [2.003, 1.940, 1.847] and a minor component (33%) with g-values = [1.990, 1.959, 1.880]. Model 1, fits the spectra better than model 2, which is also consistent with the parameters reported by Huynh et al.[13]

The goal for this work is to extract the structural information of the intermediate from the hyperfine interaction (HFI) tensors A of the multiple-incorporated magnetic nuclei. These hyperfine parameters are obtained from simulations of the orientation-selected ENDOR and

HYSCORE spectra.[14] And we noted that all the orientation-selected spectra could be well simulated by using one set of HFI tensor (for each magnetic nucleus) relative to the *g*-tensor of the major component in model 1, as shown in Figure 3-6. We also compared the fitting by using the major component (*g*-values = [1.993, 1.941, 1.847]) of model 1 with the fitting by using the major component (*g*-values = [2.003, 1.940, 1.847]) of model 2, as illustrated in Figure S21, showing that model 1 is better than model 2 in terms of the breadth of ENDOR signals. Therefore, in this work we report the HFI tensors relative to the *g*-values of [1.993, 1.941, 1.847], i.e., the major component of model 1, and employ them to extract structural information of the paramagnetic intermediate.

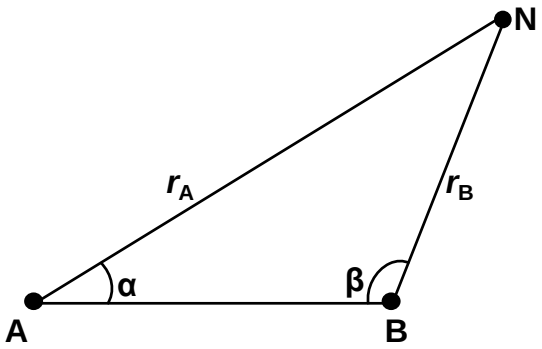

Figure S1. Geometrical definitions for extended point-dipole approximation model[15] with a nucleus (N) coupled to two exchanged-coupled spin centers A and B.

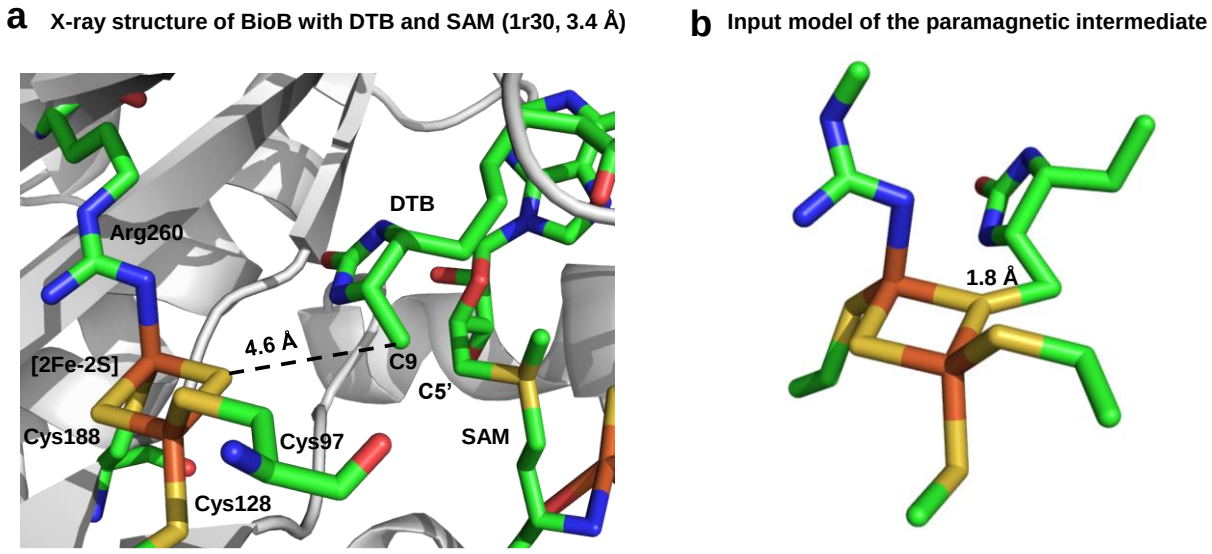

Figure S2. Input model of the paramagnetic intermediate. a, X-ray structure of BioB with DTB and SAM bound (PDB: 1r30), adapted from reference (16). The C9 of DTB is located ~4.6 Å (center-to-center) away from the nearest μ-sulfide of the oxidized $[2Fe{-}2S]^{2+}$ cluster, but in the plane bisecting the Fe−S−Fe angle with the angel of C9−S−S ~174º. **b,** The intermediate model is constructed by translating the [2Fe−2S] cluster towards the DTB by 2.8 Å to form a typical carbon-sulfur bond with bond length ~1.8 Å.

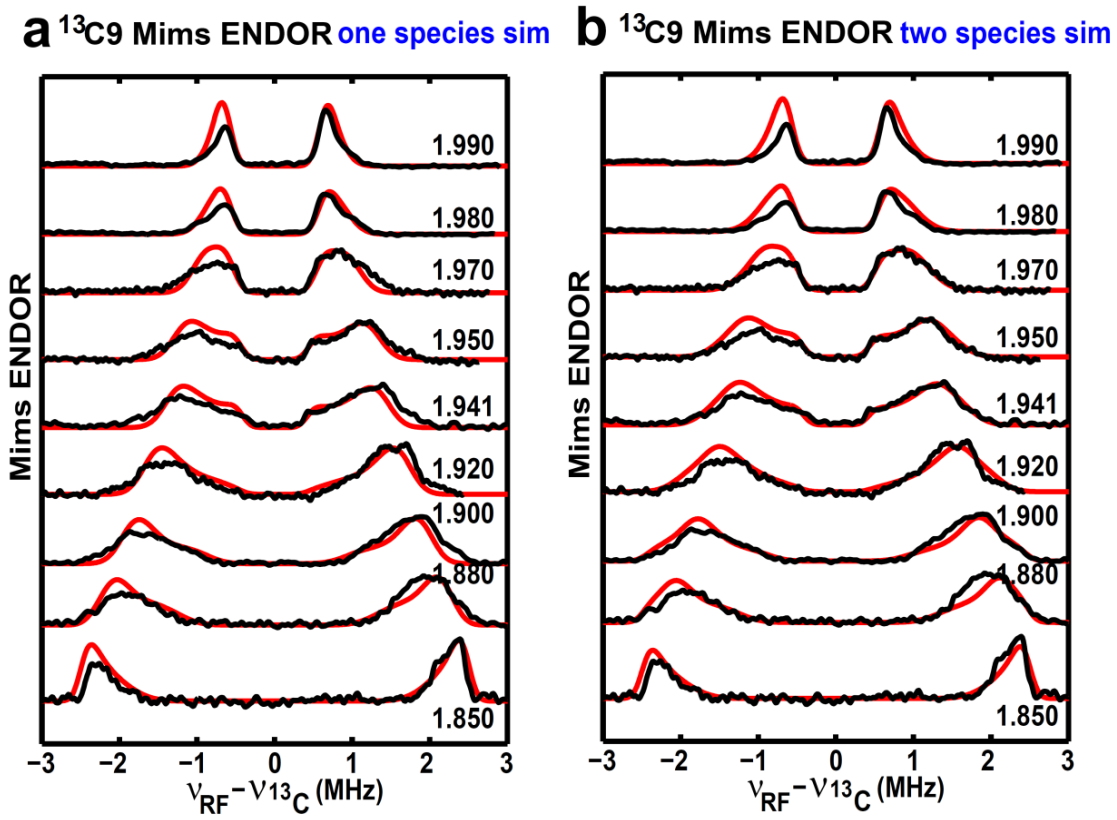

Figure S3. Simulations of the orientation-selected ^{13}C9 Mims-ENDOR spectra with one component or two components. a, Simulations by using the HFI tensor of A = [1.30, 0.85, 4.98] MHz relative to the major component g-tensor of [1.993, 1.941, 1.847] with Euler angle = [90, 11, 100]°. **b,** Simulations employing the same HFI tensor but two-component g-tensors of [1.993, 1.941, 1.847] (64%) and [2.005, 1.960, 1.881] (36%). Therefore, the simulated spectrum is the sum of two contributions: one (64%) using the HFI tensor of A = [1.30, 0.85, 4.98] MHz relative to the g-tensor of [1.993, 1.941, 1.847] with Euler angle = [90, 11, 100]°; the other (36%) using the HFI tensor of A = [1.30, 0.85, 4.98] MHz relative to the g-tensor of [2.005, 1.960, 1.881] with Euler angle = [90, 11, 100]°.

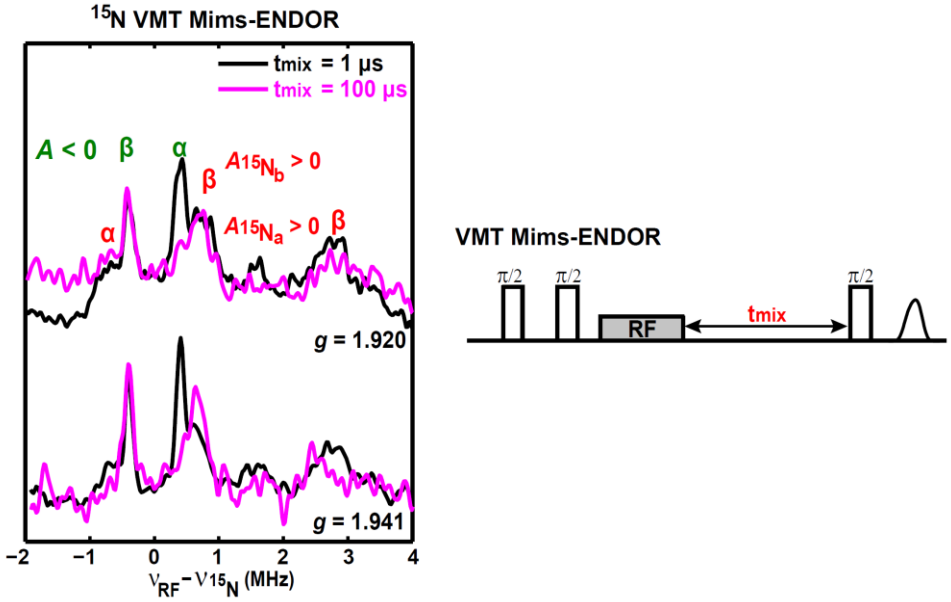

Figure S4. ^{15}N-variable mixing-time (VMT) Mims-ENDOR spectra of the intermediate with (guanidino-$^{15}N_2$)-arginine recorded at *g* = 1.941 and 1.920 and T = 10 K. For t_{mix} = 100 µs (magenta traces), the intensities of low RF frequency peak (α electron spin manifold) of $^{15}N_b$ decrease, while the corresponding high RF frequency peaks (β electron spin manifold) for $^{15}N_b$ and $^{15}N_a$ still persists, suggesting the positive hyperfine couplings for both $^{15}N_b$ and $^{15}N_a$. On the contrary, for the third ^{15}N (labeled as green), the intensity of high RF frequency peak decreases dramatically as increasing the t_{mix} from 1 µs to 100 µs, suggesting a negative hyperfine coupling for this ^{15}N (*see* also the green shades in Figure 3E & 3F).

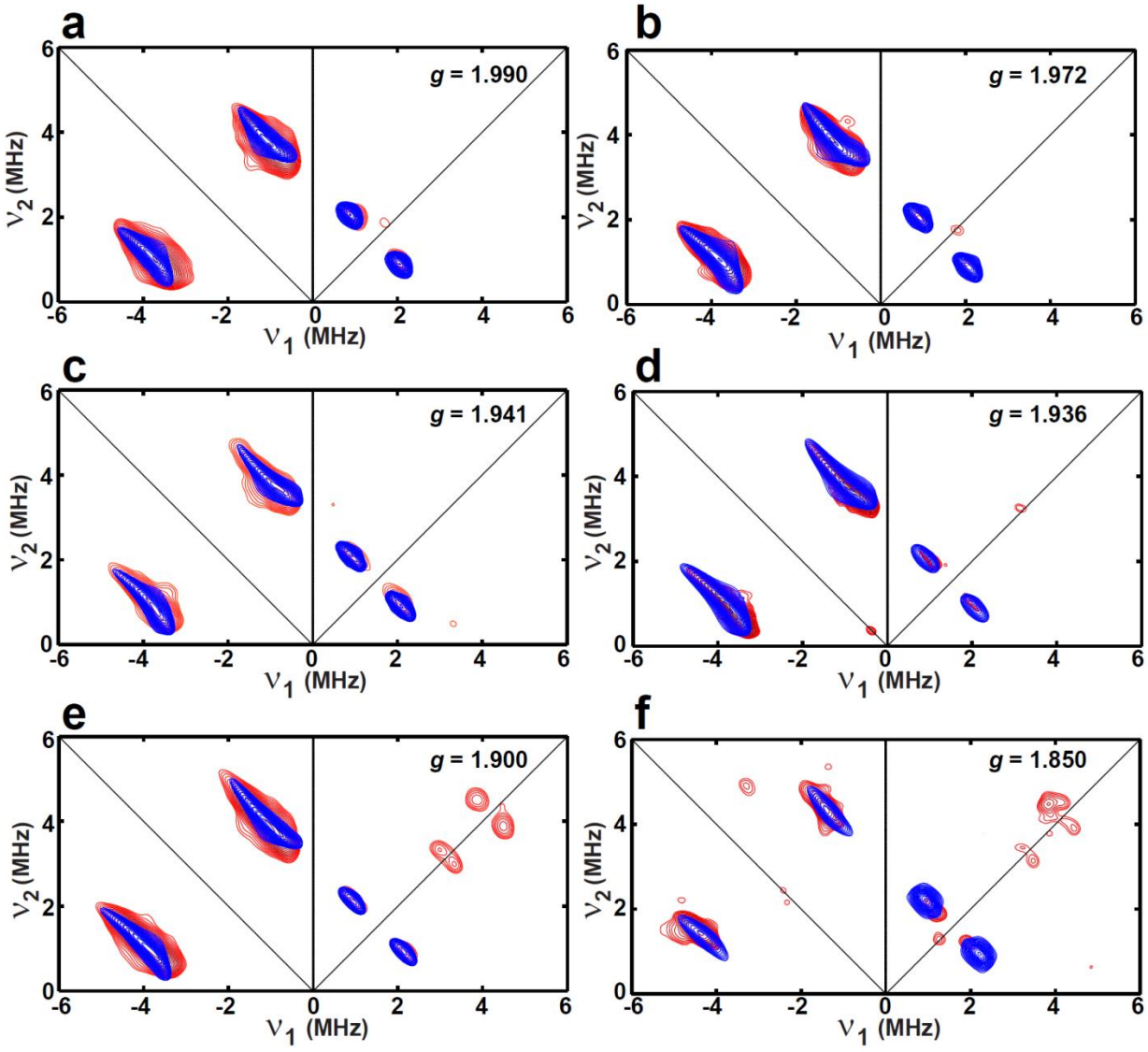

Figure S5. Orientation-selected X-band HYSCORE spectra of the paramagnetic intermediate with (guanidino-$^{15}N_2$)-arginine. Experimental parameters: temperature = 10 K; $t_{\pi/2}$ = 16 ns; t_{π} = 32 ns; and microwave frequency = 9.476 GHz; magnetic field = 340.2 mT; τ = 140 ns (**a**); microwave frequency = 9.476 GHz; magnetic field = 343.3 mT; τ = 136 ns (**b**); microwave frequency = 9.418 GHz; magnetic field = 347.5 mT; τ = 136 ns (**c**); microwave frequency = 9.490 GHz; magnetic field = 349.3 mT; τ = 180 ns (**d**); microwave frequency = 9.476 GHz; magnetic field = 356.3 mT; τ = 132 ns (**e**); microwave frequency = 9.444 GHz; magnetic field = 364.9 mT; τ = 180 ns (**f**). The time increment in both dimensions was 24 ns with 180 steps. The experimental spectra (contour plot) are in red and the simulated spectra are in blue. Simulations employed three ^{15}N species: two ($^{15}N_a$ and $^{15}N_b$) are from the guanidino group of Arg260, the third one is possibly from Arg95; the parameters are given in the caption of Figure 3.

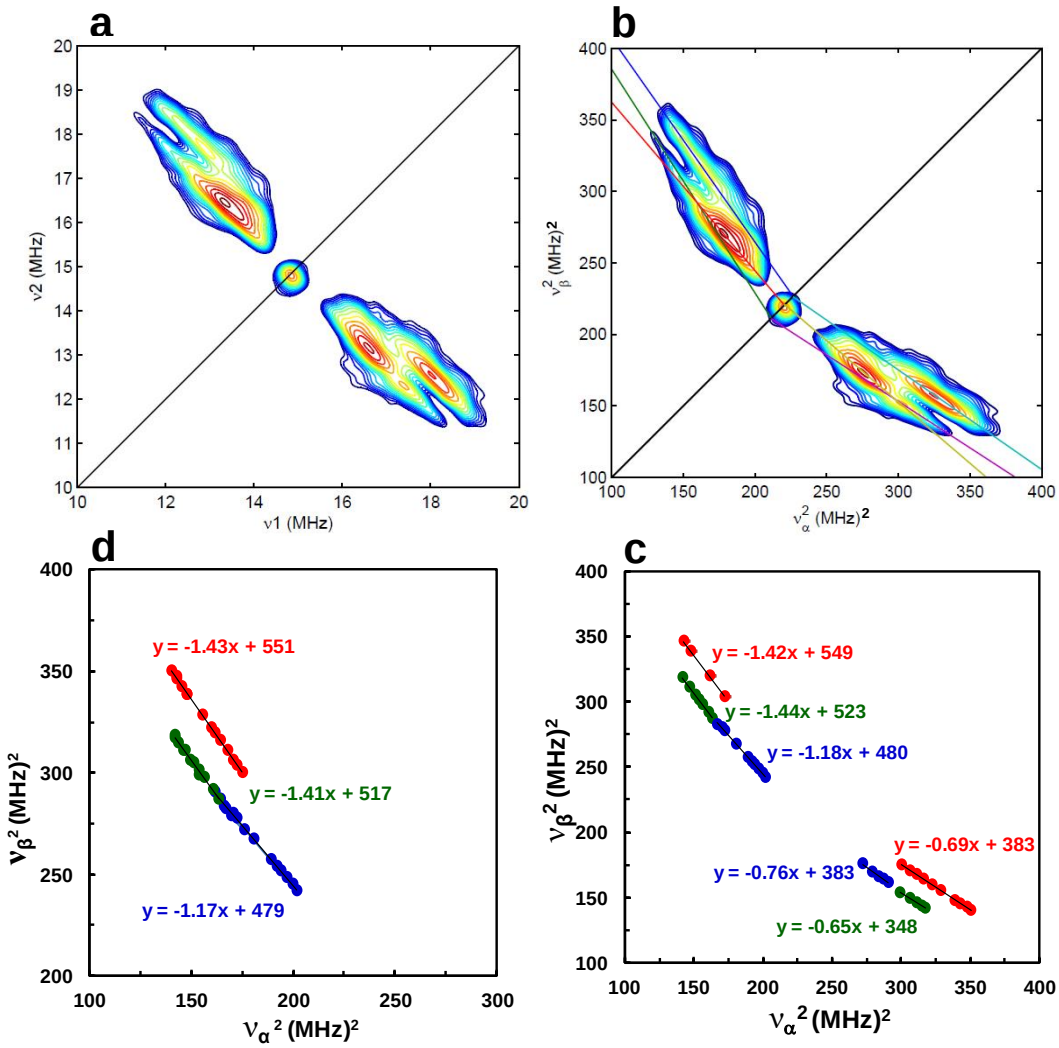

Figure S6. Illustration of using Dikanov's method to extract different sets of beta-proton based on the contour lineshape of HYSCORE spectra. a, X-band (9.428 GHz) ^{1}H-HYSCORE spectrum of the paramagnetic intermediate recorded at 348.0 mT (corresponding to g = 1.935), where the ^{1}H Larmor frequency is 14.82 MHz. Experimental parameters: temperature = 10 K; $t_{\pi/2}$ = 16 ns; t_π = 16 ns; τ = 204 ns. **b,** HYSCORE spectra shown in **a** is plotted as ν_α^2 versus ν_β^2, and then the contour line shape is transformed into a straight line. Three sets of straight line with distinct slopes and intercepts are extracted and presented in **d**.

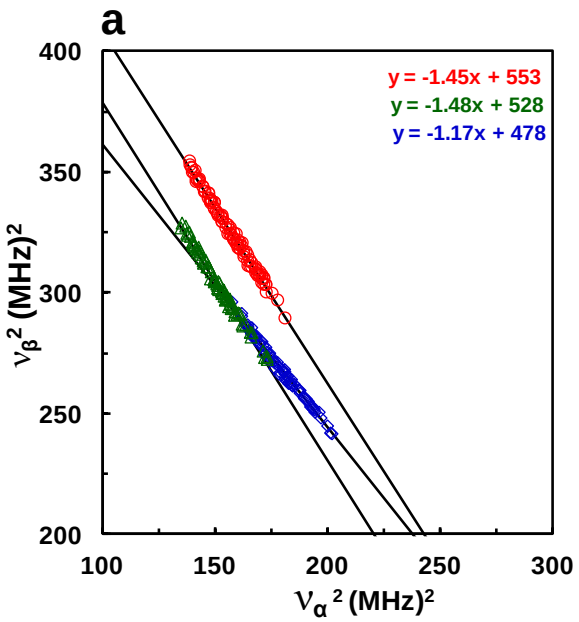

b Extracted three sets of proton ^{1}H

Set of ^{1}H	Slope Q	Intercept G/MHz^2	Hyperfine a_{iso}/MHz	Hyperfine T/MHz
1	-1.45±0.02	553±5	3.04±0.3 -7.95±0.3	4.9±0.6
2	-1.48±0.06	528±10	4.9±2.0 -7.13±2.0	1.6±2.3
3	-1.17±0.02	478±3	1.32±0.4 -3.29±0.4	1.9±0.8

Figure S7. The extracted three sets of beta-protons of the paramagnetic intermediate. a, Three straight lines are obtained from the data points (ν_α, ν_β) recorded at five magnetic fields corresponding to g values of 1.993, 1.983, 1.947, 1.935 and 1.909 and normalized to 14.82 MHz (the ^{1}H Larmor frequency 348.0 mT) via eq. S2. Each line contains >100 data points. **b**, Three sets of axial hyperfine coupling are computed via eq. S1 by using the slopes and intercepts obtained from **a**.

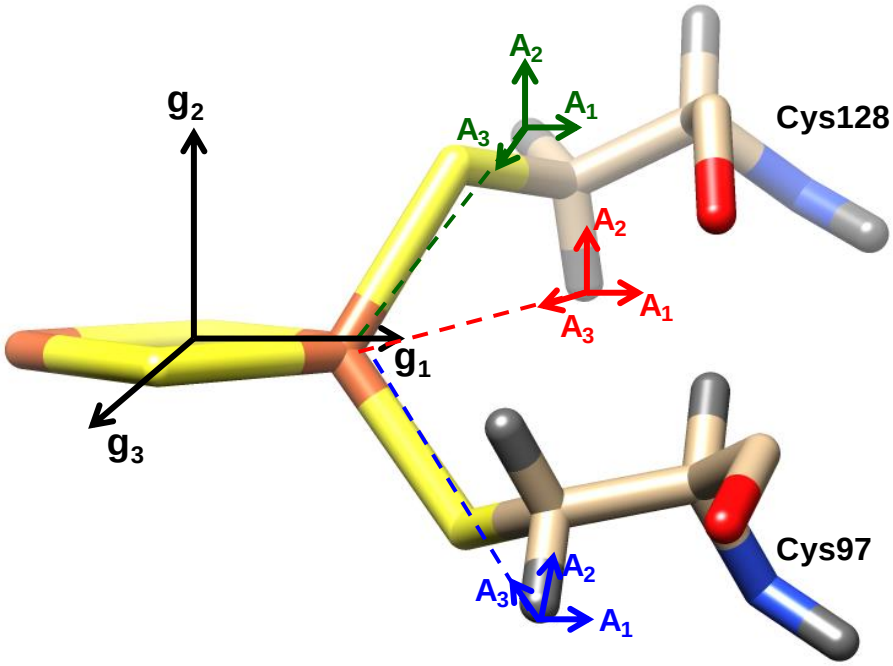

Figure S8. Assignment of three beta-protons. The HFI tensors for three beta-protons are $A(^1H1, red)$ = [-1.07, -1.07, 13.86] MHz, Euler angle = [0, -36, 0]°; $A(^1H2, green)$ = [-1.70, -1.70, 10.05] MHz, Euler angle = [0, -5, 0]°; $A(^1H3, blue)$ = [-0.65, -0.65, 5.84] MHz, Euler angle = [0, -95, 30]°. g_1 is generally believed to be along the Fe-Fe internuclear vector (for Rieske and MitoNEET, *see* Table 1 for *g*-tensor frames in details).

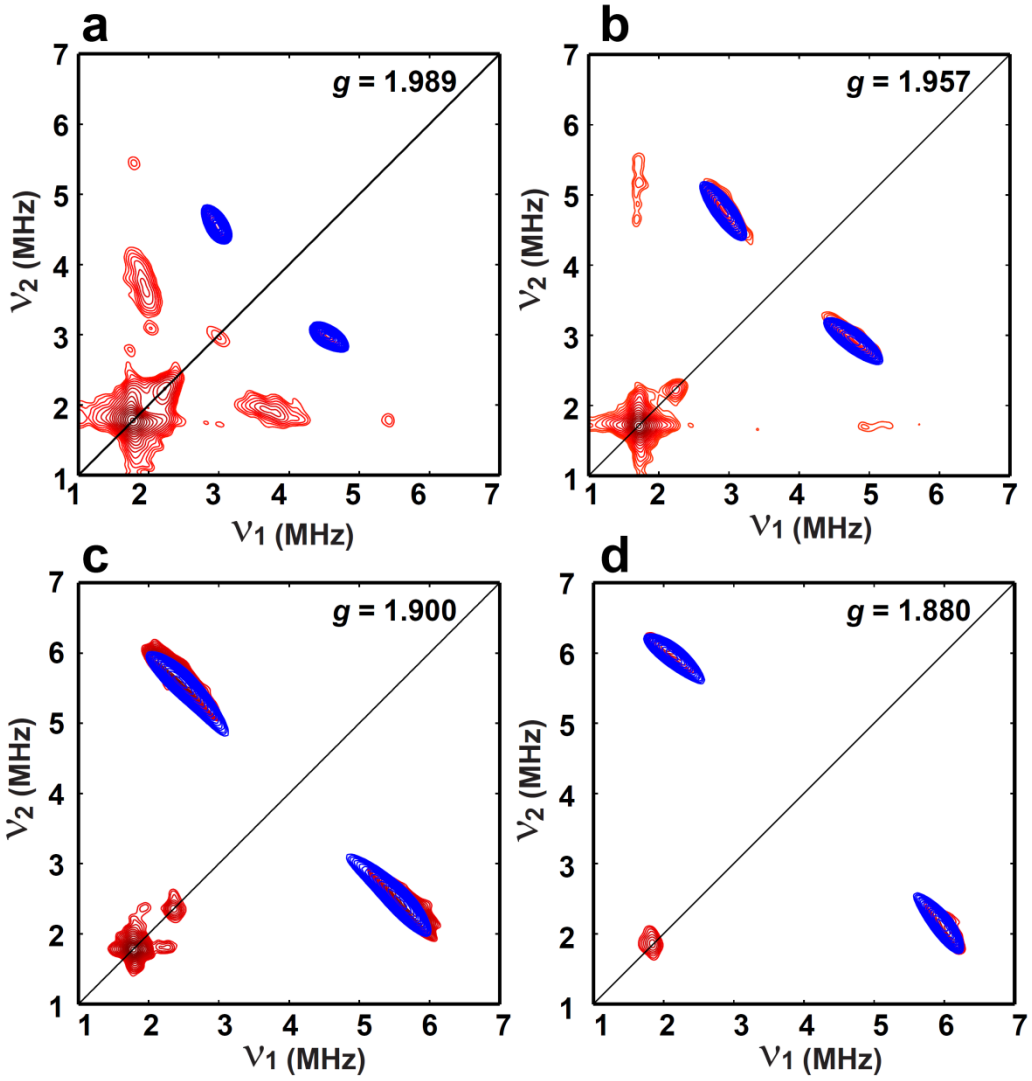

Figure S9. Orientation-selected X-band HYSCORE spectra of the paramagnetic intermediate generated by using ^{13}C9-DTB. Experimental parameters: temperature = 10 K; $t_{\pi/2}$ = 16 ns; t_{π} = 16 ns; and microwave frequency = 9.743GHz; magnetic field = 350.0 mT; τ = 132 ns (**a**); microwave frequency = 9.727 GHz; magnetic field = 355.0 mT; τ = 132 ns (**b**); microwave frequency = 9.727 GHz; magnetic field = 365.0 mT; τ = 128 ns (**c**); microwave frequency = 9.740 GHz; magnetic field = 370.0 mT; τ = 208 ns (**d**). The time increment in both dimensions was 20 ns with 180 steps. The experimental spectra (contour plot) are in red which are adapted from reference (1), while the simulated spectra are in blue with the updated hyperfine coupling parameters given in the caption of Figure 5.

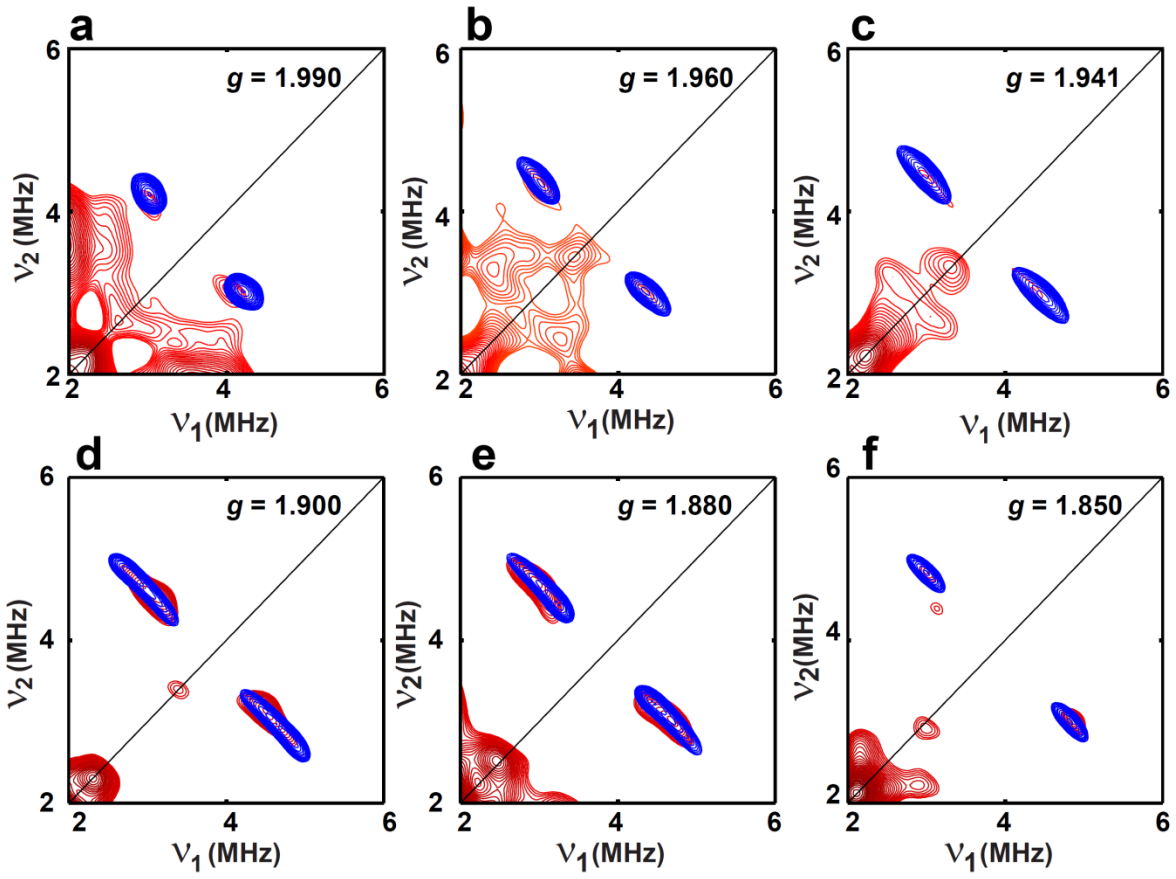

Figure S10. Orientation-selected X-band HYSCORE spectra of the paramagnetic intermediate generated by using ^{13}C8-DTB. Experimental parameters: temperature = 10 K; $t_{\pi/2}$ = 16 ns; t_{π} = 32 ns; and microwave frequency = 9.428 GHz; magnetic field = 338.7 mT; τ = 140 ns (**a**); microwave frequency = 9.445 GHz; magnetic field = 344.3 mT; τ = 136 ns (**b**); microwave frequency = 9.428 GHz; magnetic field = 347.0 mT; τ = 132 ns (**c**); microwave frequency = 9.445 GHz; magnetic field = 355.0 mT; τ = 132 ns (**d**); microwave frequency = 9.445 GHz; magnetic field = 358.9 mT; τ = 132 ns (**e**); microwave frequency = 9.445 GHz; magnetic field = 364.7 mT; τ = 128 ns (**f**). The time increment in both dimensions was 24 ns with 180 steps. The experimental spectra (contour plot) are in red, while the simulated spectra are in blue using the hyperfine coupling parameters given in the caption of Figure 5.

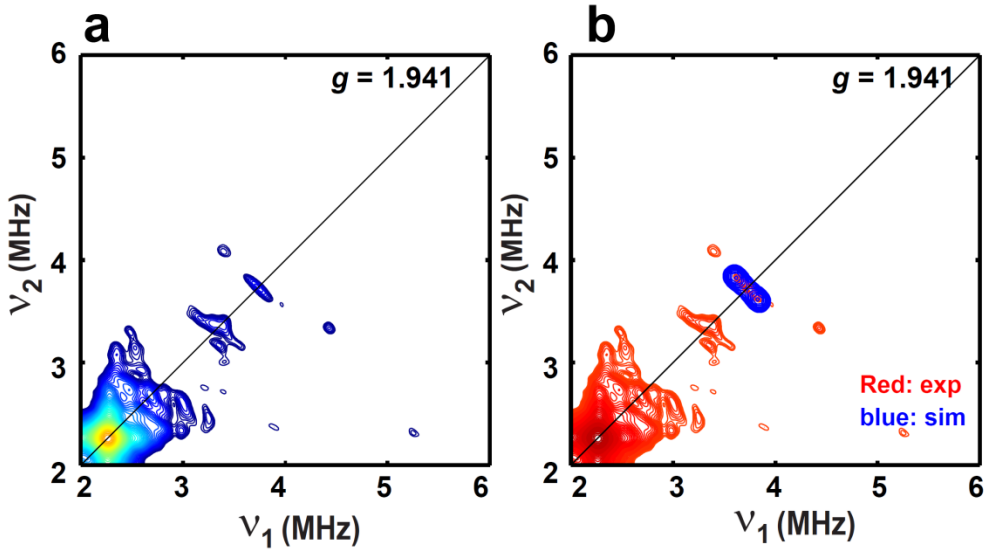

Figure S11. X-band HYSCORE spectra of the paramagnetic intermediate generated by using ^{13}C10-DTB. a, Experimental spectra recorded at g = 1.941. The other parameters are temperature = 10 K; $t_{\pi/2}$ = 16 ns; t_{π} = 32 ns; and microwave frequency = 9.496 GHz; magnetic field = 349.5 mT; τ = 136 ns. The time increment in both dimensions was 24 ns with 400 steps. **b,** Simulation (blue contour) of ^{13}C10 HYSCORE spectrum employed the parameters given in the caption of Figure 5.

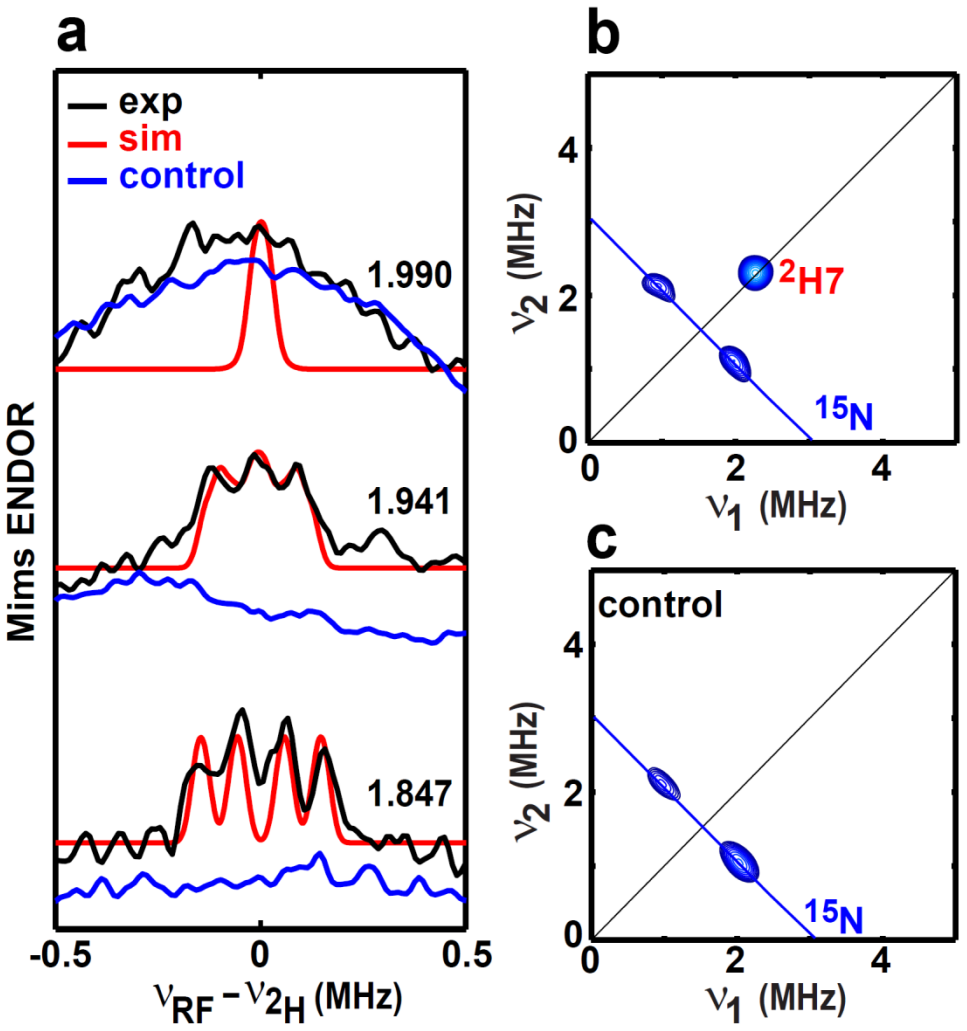

Figure S12. Q-band Mims-ENDOR and X-band HYSCORE spectra of the paramagnetic intermediate generated by using ^{2}H7-DTB and BioB with (guanidino-$^{15}N_2$)-arginine. a, Orientation-selected Mims-ENDOR spectra of ^{2}H7 (black traces) recorded at *g* values of 1.990, 1.941 and 1.847. The control sample in **a** and **c** is the paramagnetic intermediate generated by using natural abundance DTB and BioB with (guanidino-$^{15}N_2$)-arginine. As there is signal arising from strong coupling $^{15}N_a$ around the ^{2}H larmor frequency for both black and blue traces, it is difficult to extract the signal from just ^{2}H at g = 1.990. However, from the spectra recorded at two other *g* values, we are able to extract the hyperfine coupling parameters as well as the quadrupole coupling for ^{2}H7, which are given in the caption of Figure 6. **b,** X-band HYSCORE spectrum of the intermediate with both ^{2}H7 and (guanidino-$^{15}N_2$)-arginine, while the control spectrum with only ^{15}N hyperfine signals are shown in **c**.

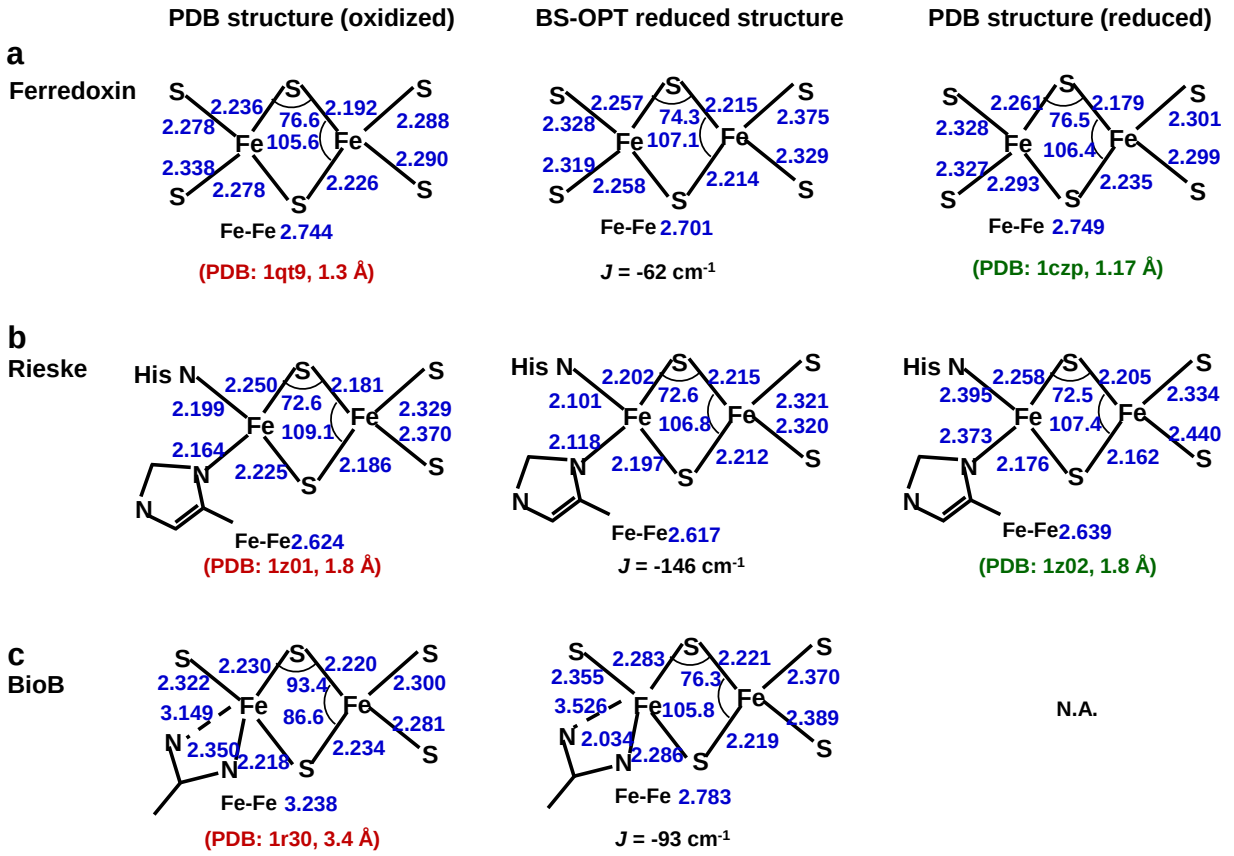

Figure S13. Comparison of the geometry of reduced [2Fe−2S] clusters obtained from BS-DFT optimization and the geometry obtained from X-ray crystallography. a, Three structures of the [2Fe−2S] cluster in ferredoxin. **b,** Three structures of the [2Fe−2S] cluster in Rieske. **c,** Two structures of the auxiliary [2Fe−2S] cluster in BioB.

a Optimized geometry

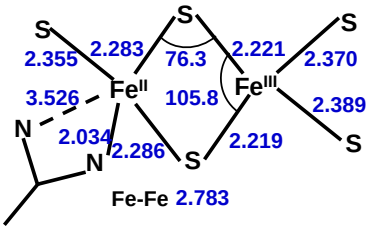

b Löwdin spin distribution

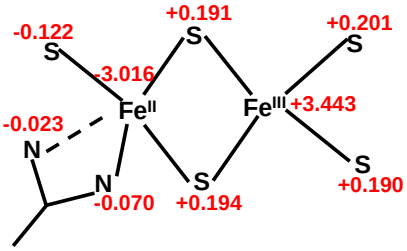

c Spin distribution of three models and corresponding projection factors K^A and K^B

Atom	Model 1			Model 2 (Noodleman's)[a]				Model 3 (BioB)			
	ρ^A	K^A	d^A	ρ^A	$\rho^{A,\,sum}$	K^A	d^A	ρ^A	$\rho^{A,\,sum}$	K^A	d^A
Fe^{3+}	5	7/3	1	+3.256			0.819	+3.443			0.807
S*			0	+0.174	+4.033	+2.011	0.044	+0.194	+4.262	+2.088	0.045
S_{ox}			0	+0.187			0.047	+0.201			0.047
	ρ^B	K^B	d^B	ρ^B	$\rho^{B,\,sum}$	K^B	d^B	ρ^B	$\rho^{B,\,sum}$	K^B	d^B
Fe^{2+}	-4	-4/3	1	-2.874	-3.033	-1.011	0.934	-3.016	-3.262	-1.088	0.924
S_{red}			0	-0.100			0.033	-0.122			0.037
N_a								-0.070			0.021
N_b								-0.023			0.007

[a]L. Noodleman, C. Y. Peng, D. A. Case and J. M. Mouesca, *Coord. Chem. Rev.*, 1995, 144, 199.

Figure S14. Optimized geometry and Löwdin spin distribution of the reduced [2Fe−2S] cluster in BioB. The calculated spin projection factors are given in **c.**

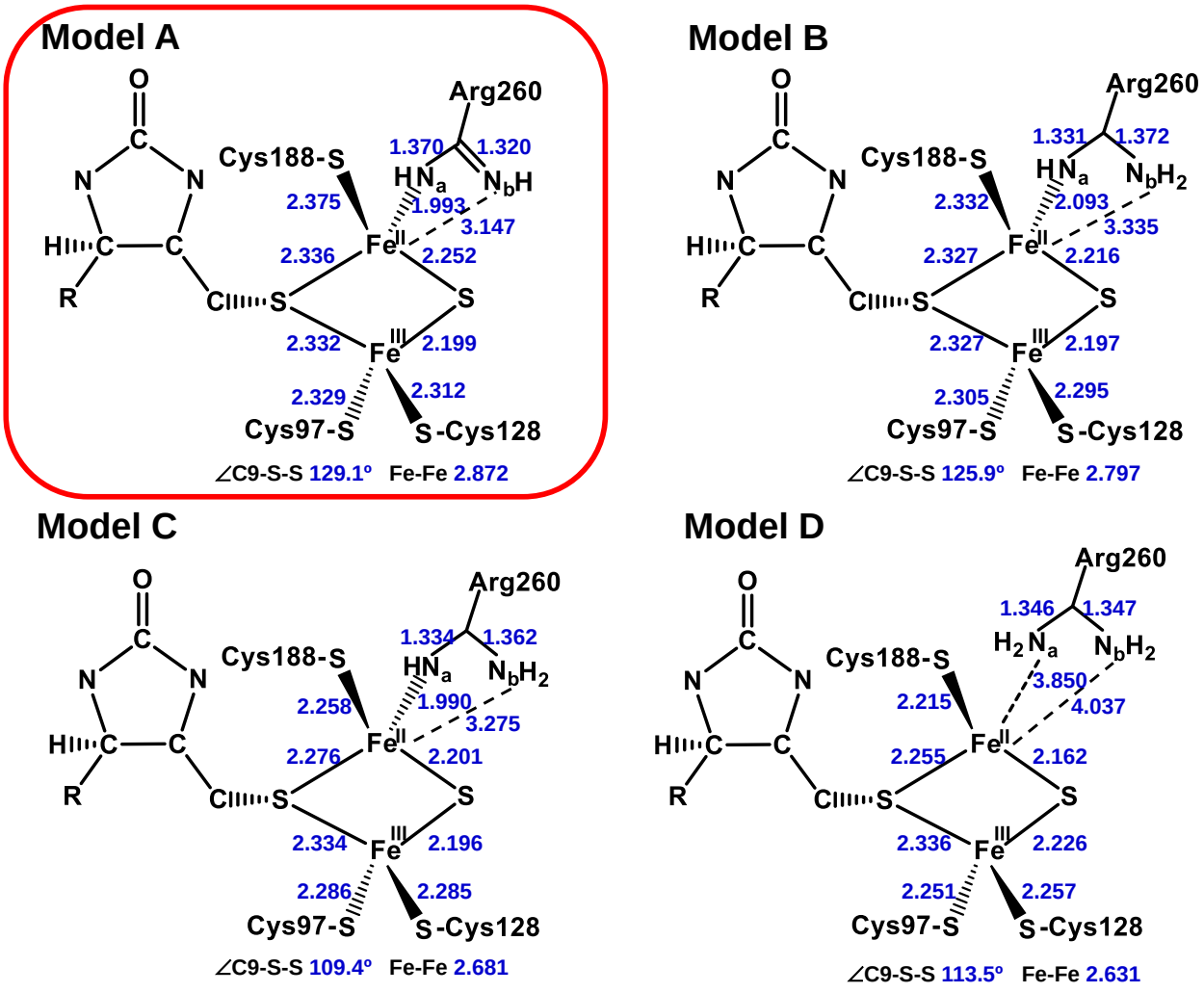

Model	M_s of BS state	Charge	Protonation state of guanidino group	Fe coordinated with guanidino group
A	1/2	-2	-HNC(=NH)NHCH$_3$	ferrous
B	1/2	-1	-HNC(-NH$_2$)NHCH$_3$	ferrous
C	1/2	-1	-H$_2$NC(-NH)NHCH$_3$	ferrous
D	1/2	0	-H$_2$NC(-NH$_2$)NHCH$_3$	ferrous

Figure S15. Optimized geometry of four models (A, B, C and D) of the intermediate with various protonation states of guanidino group. Model A is also presented in Figure 7A & 8B.

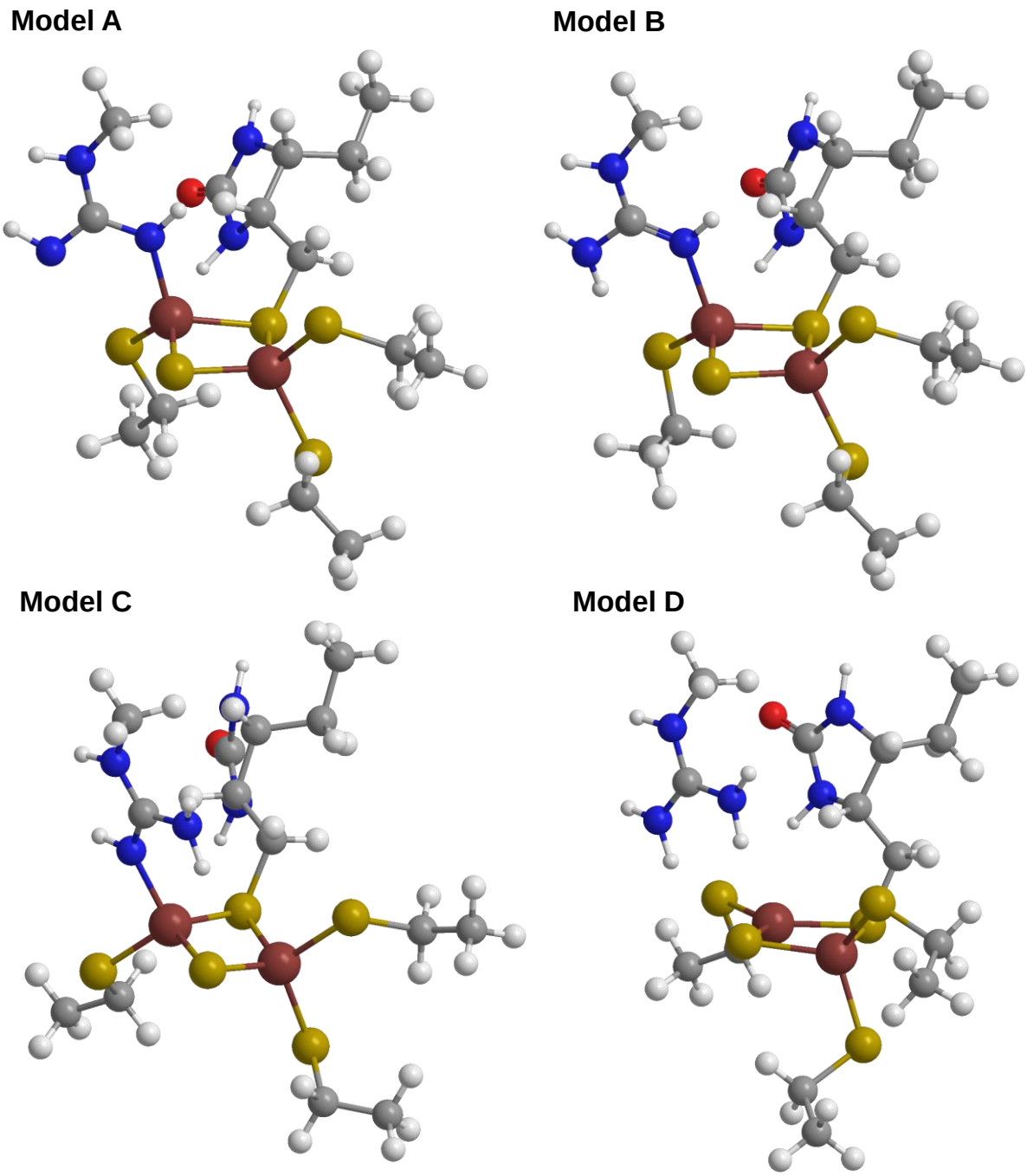

Figure S16. Ball-and-stick model of the optimized geometry of four models (A, B, C and D) of the intermediate with various protonation states of guanidino group. Model A is also presented in Figure 7A & 8B.

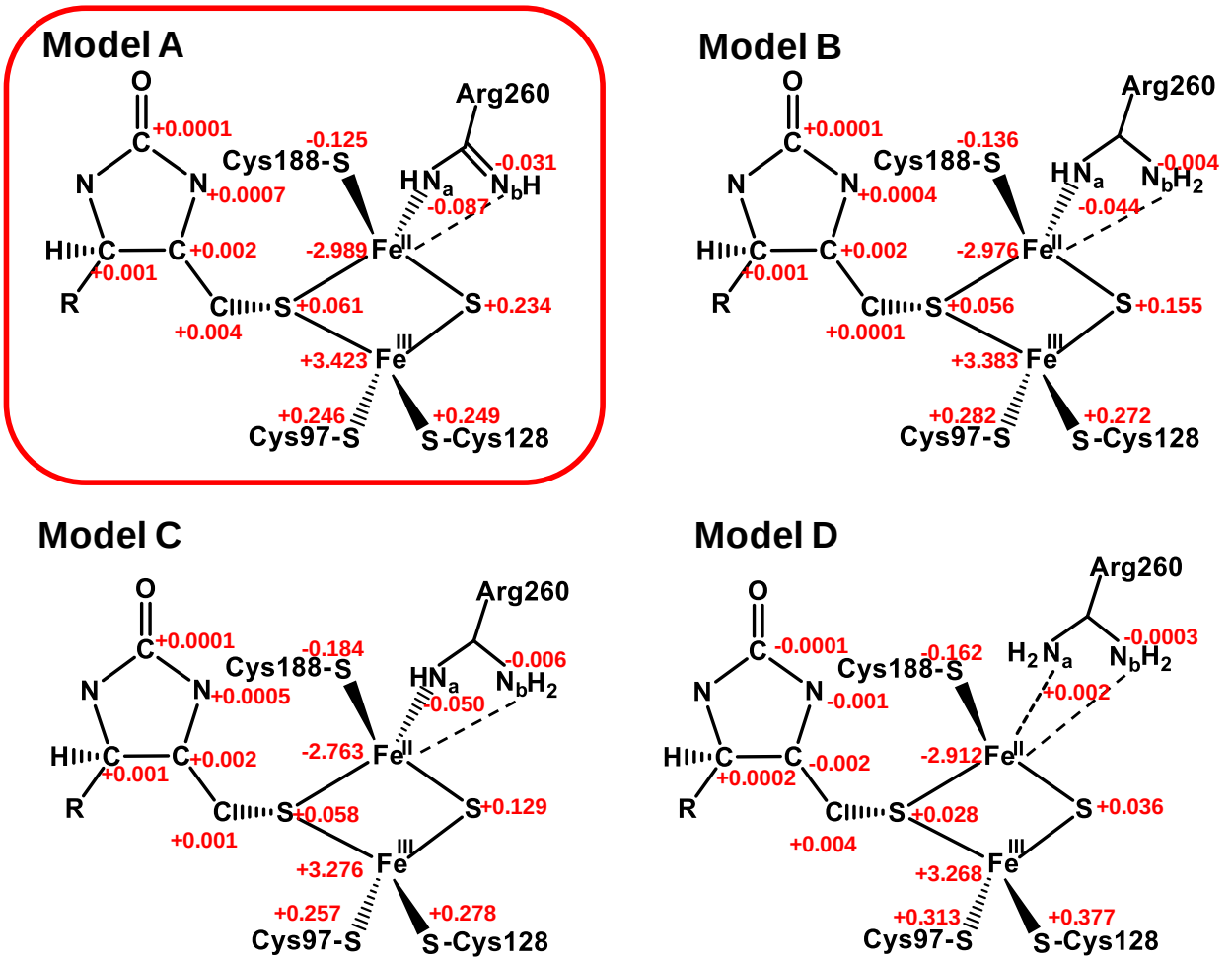

Figure S17. Löwdin spin distributions over four models (A, B, C and D) of the intermediate with the corresponding geometry given in Figure S15 & S16.

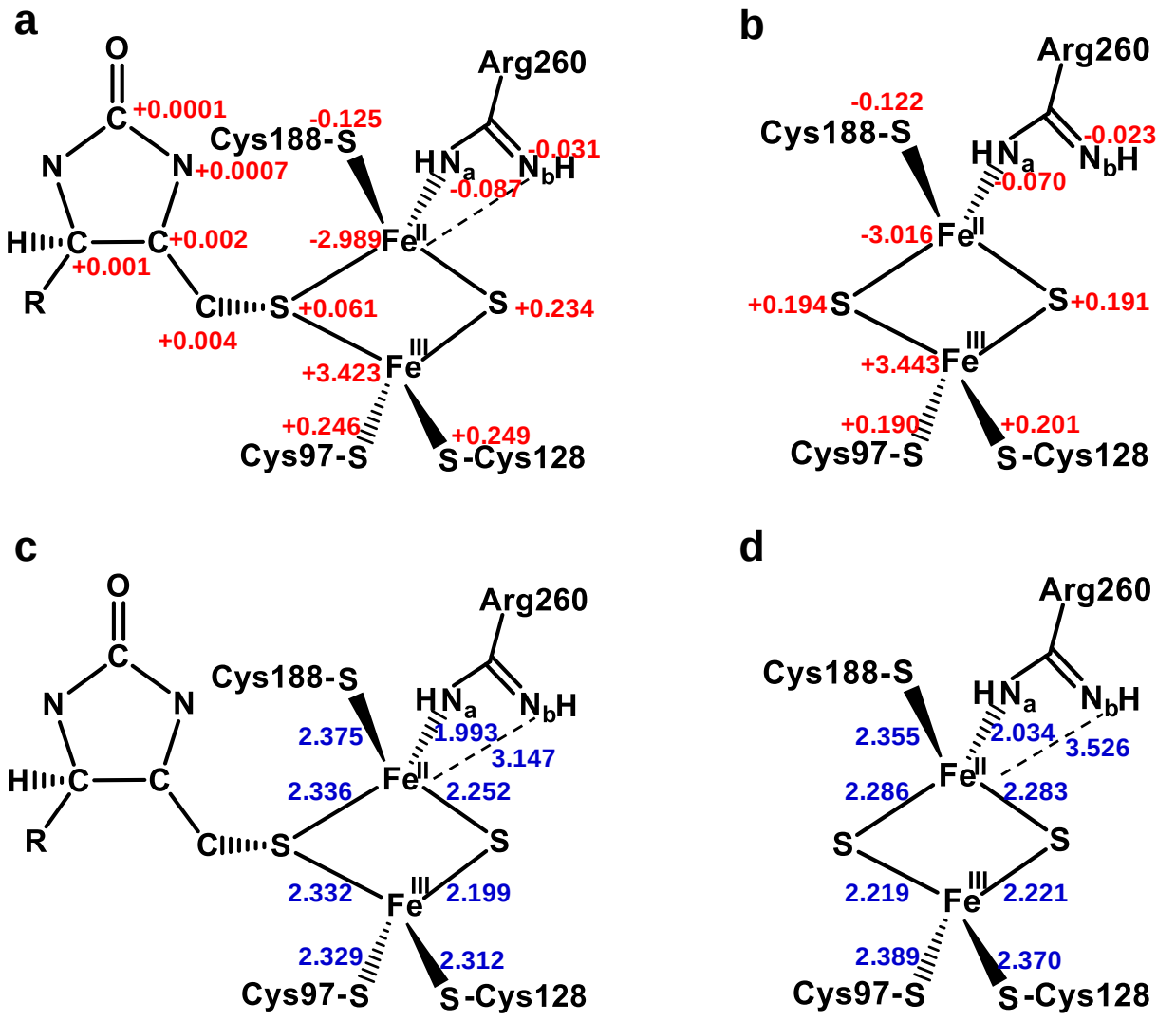

Figure S18. Comparison of spin distribution and geometry between the intermediate and the reduced [2Fe−2S] cluster in BioB. a, Spin distribution over the intermediate model A, with the corresponding geometry shown in **c** and Figure S15 & S16. **b,** Spin distribution over the reduced [2Fe−2S] cluster, with the corresponding geometry shown in **d** and Figure S13.

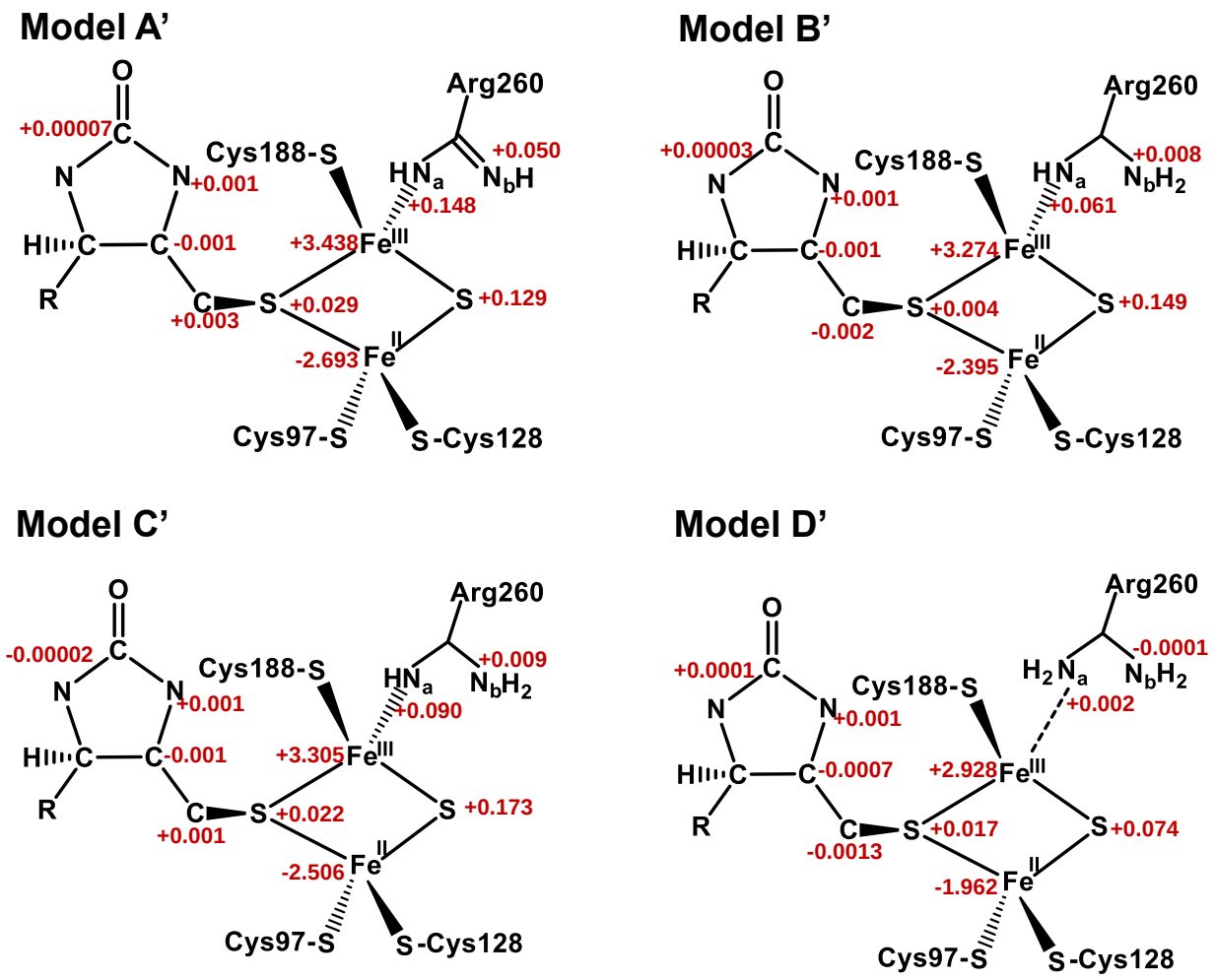

Model	M_s of BS state	Charge	Protonation state of guanidino group	Fe coordinated with guanidino group
A'	1/2	-2	$-HNC(=NH)NHCH_3$	ferric
B'	1/2	-1	$-HNC(-NH_2)NHCH_3$	ferric
C'	1/2	-1	$-H_2NC(-NH)NHCH_3$	ferric
D'	1/2	0	$-H_2NC(-NH_2)NHCH_3$	ferric

Figure S19. Löwdin spin distributions over four models (A', B', C' and D'). These four models have the same input coordinates as the four models shown in Figure S15, with the only difference as assigning guanidino group coordinated to the ferric site.

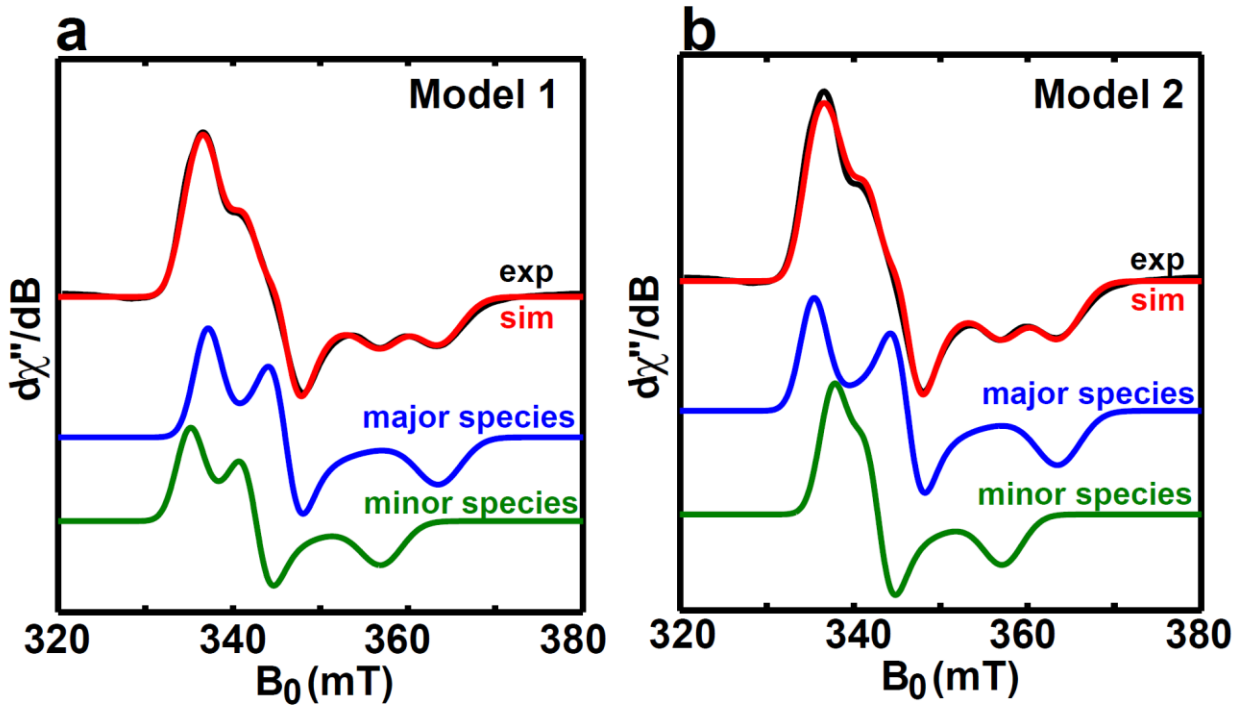

	g-values of major species	*g*-values of minor species
Model 1	[1.993, 1.941, 1.847] 64%	[2.005, 1.960, 1.881] 36%
Model 2	[2.003, 1.940, 1.847] 67%	[1.990, 1.959, 1.880] 33%

Figure S20. Two models used to simulate the EPR spectra of the paramagnetic intermediate. a, Simulation of X-band CW EPR spectrum of the intermediate by using model 1. Experimental parameters: temperature = 40 K; microwave frequency = 9.38 GHz; microwave power = 100 mW; modulation amplitude = 0.8 mT. **b,** Simulation of X-band CW EPR spectrum of the intermediate by using model 2. The black traces are experimental spectra, while the red traces are the simulated spectra involving the contributions from both major component (blue) and the minor component (green) with the ratio shown in the figure.

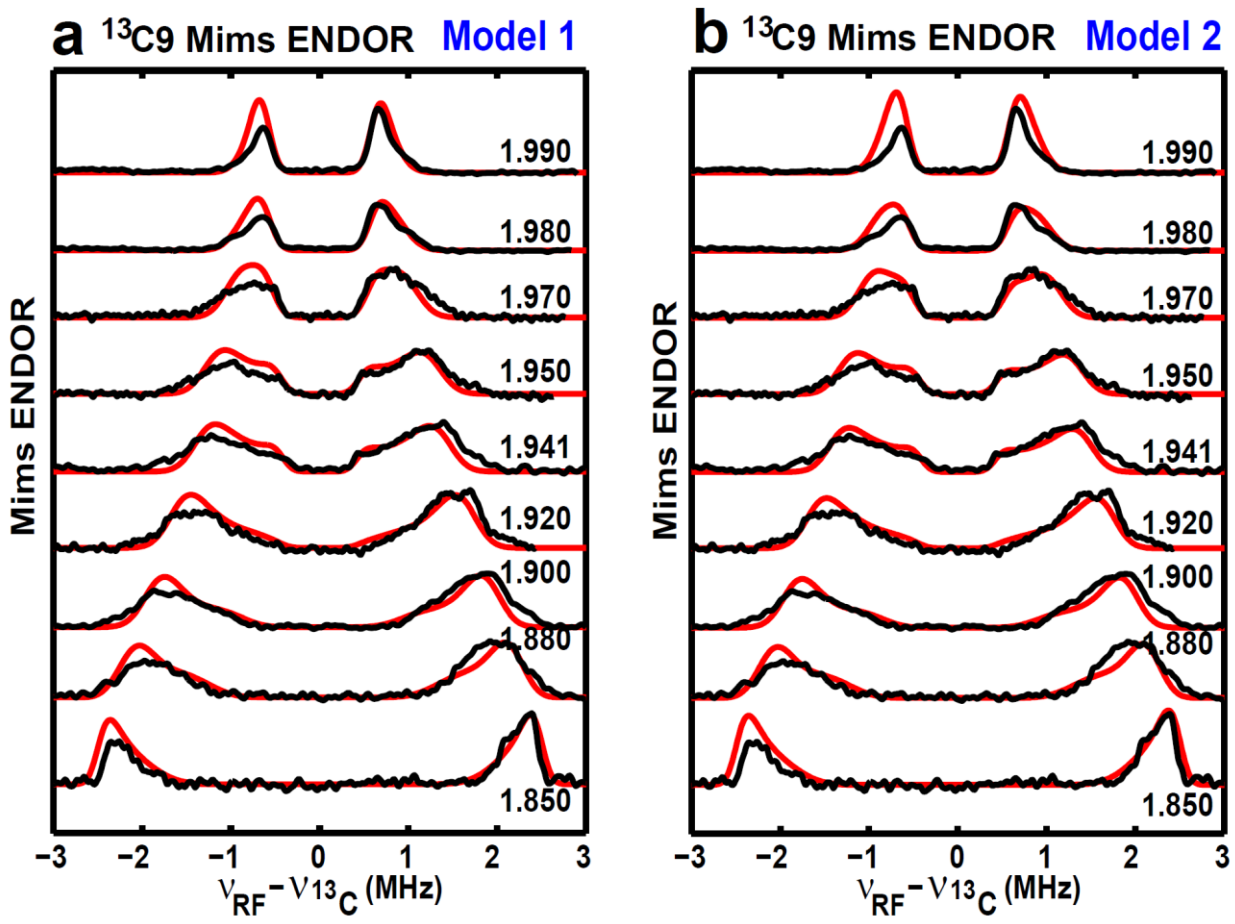

Figure S21. Simulations of the orientation-selected ^{13}C9 Mims-ENDOR spectra by using the *g*-tensor of the major-component of Model 1 or Model 2. a, Simulations by using the HFI tensor of *A* = [1.30, 0.85, 4.98] MHz relative to the *g*-tensor of [1.993, 1.941, 1.847] (the major component in model 1) with Euler angle = [90, 11, 100]°. **b,** Simulations by using the HFI tensor of *A* = [1.30, 0.85, 4.98] MHz relative to the *g*-tensor of [2.003, 1.940, 1.847] (the major component in model 2) with Euler angle = [90, 11, 100]°.

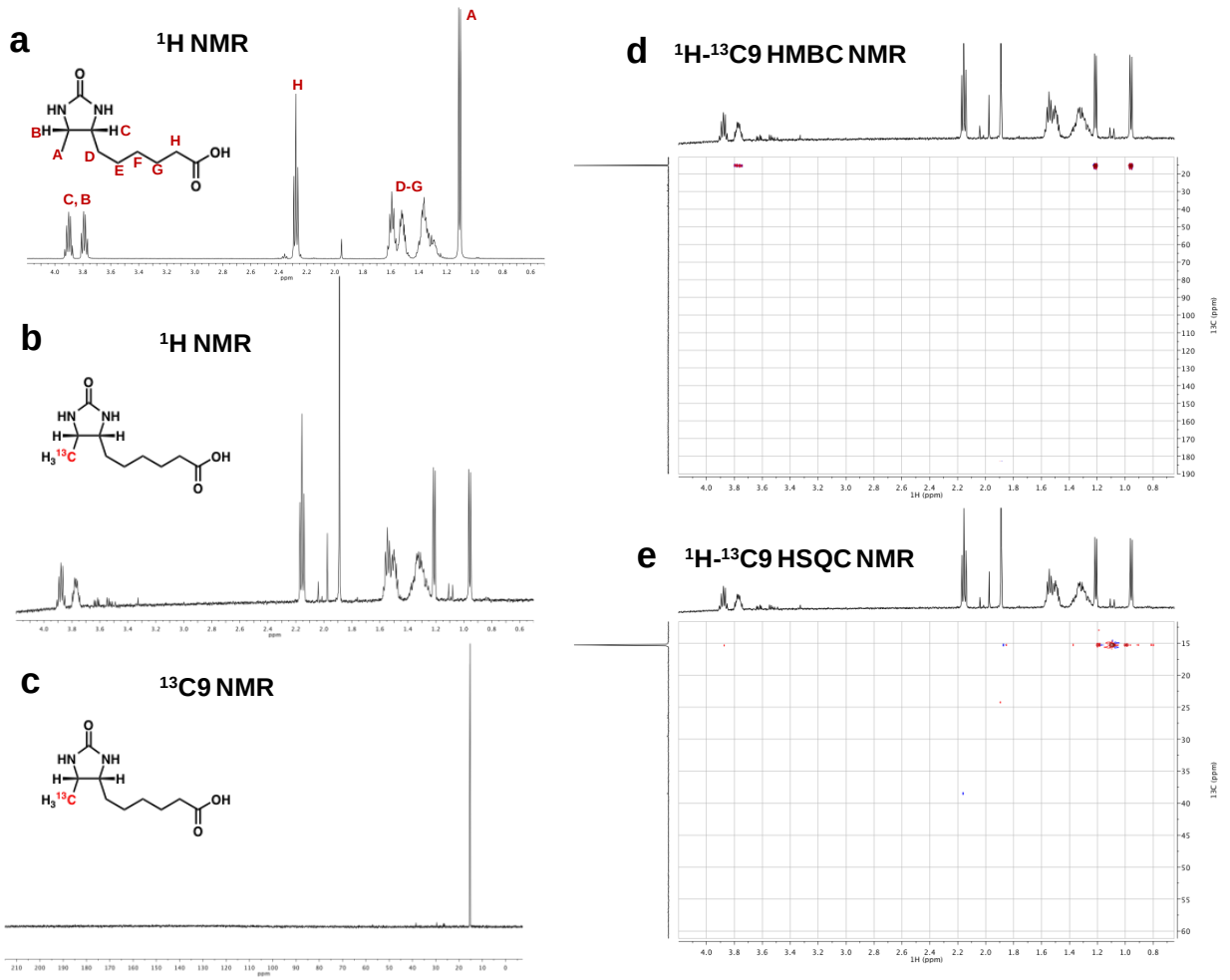

Figure S22. NMR spectra of ^{13}C9-DTB. a, ^{1}H NMR spectrum of natural abundance DTB at 500 MHz in D_2O. **b,** ^{1}H NMR spectrum of ^{13}C9-DTB at 500 MHz in D_2O. **c,** ^{13}C NMR spectrum of ^{13}C9-DTB at 125 MHz in D_2O. **d,** ^{1}H-^{13}C HMBC NMR spectra of ^{13}C9-DTB at 500 MHz in D_2O. **e,** ^{1}H-^{13}C HSQC NMR spectra of ^{13}C9-DTB at 500 MHz in D_2O.

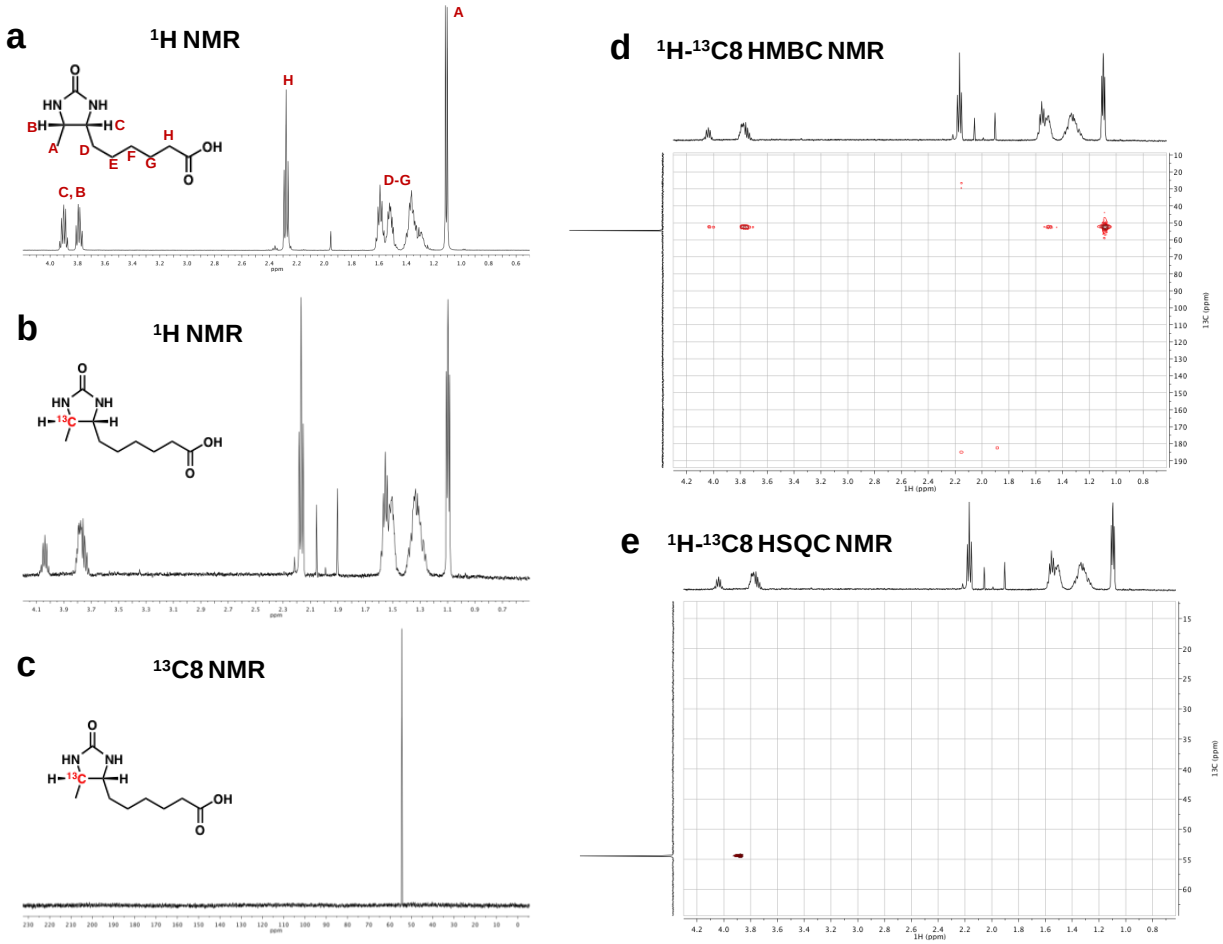

Figure S23. NMR spectra of ^{13}C8-DTB. a, ^{1}H NMR spectrum of natural abundance DTB at 500 MHz in D_2O. **b,** ^{1}H NMR spectrum of ^{13}C8-DTB at 500 MHz in D_2O. **c,** ^{13}C NMR spectrum of ^{13}C8-DTB at 125 MHz in D_2O. **d,** ^{1}H-^{13}C HMBC NMR spectra of ^{13}C8-DTB at 500 MHz in D_2O. **e,** ^{1}H-^{13}C HSQC NMR spectra of ^{13}C8-DTB at 500 MHz in D_2O.

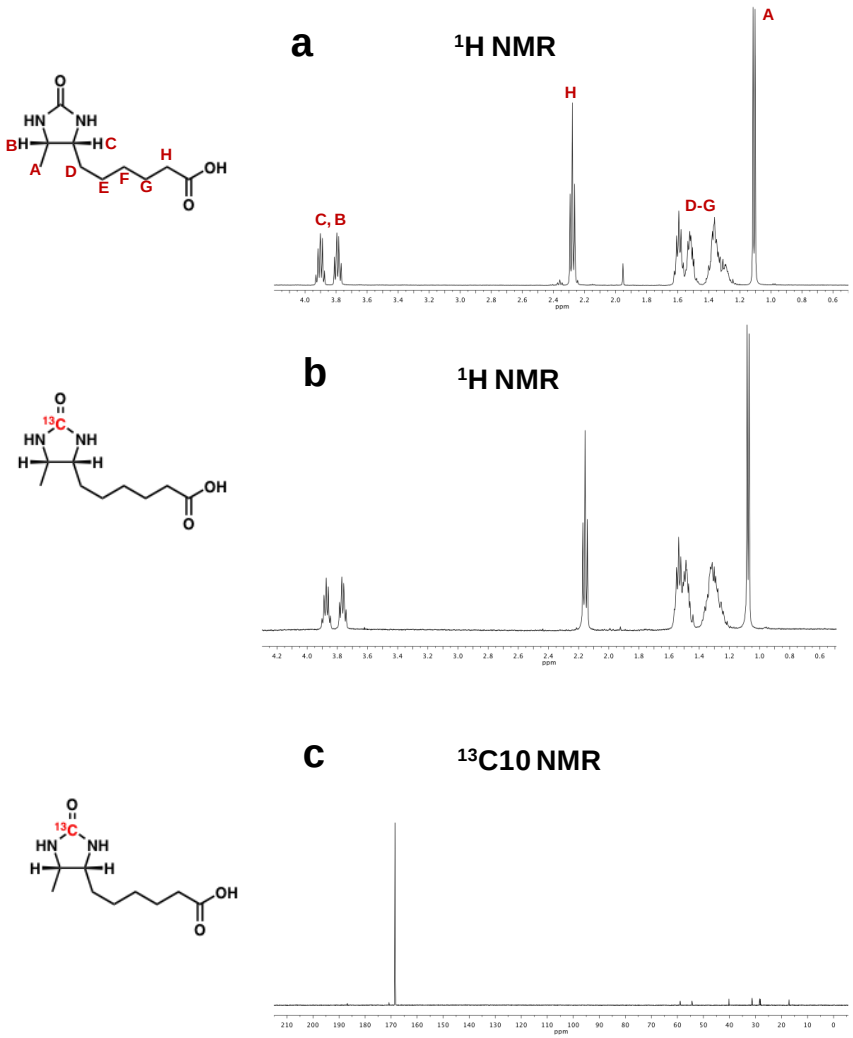

Figure S24. NMR spectra of ^{13}C10-DTB. a, ^{1}H NMR spectrum of natural abundance DTB at 500 MHz in D_2O. **b,** ^{1}H NMR spectrum of ^{13}C10-DTB at 500 MHz in D_2O. **c,** ^{13}C NMR spectrum of ^{13}C10-DTB at 125 MHz in D_2O.

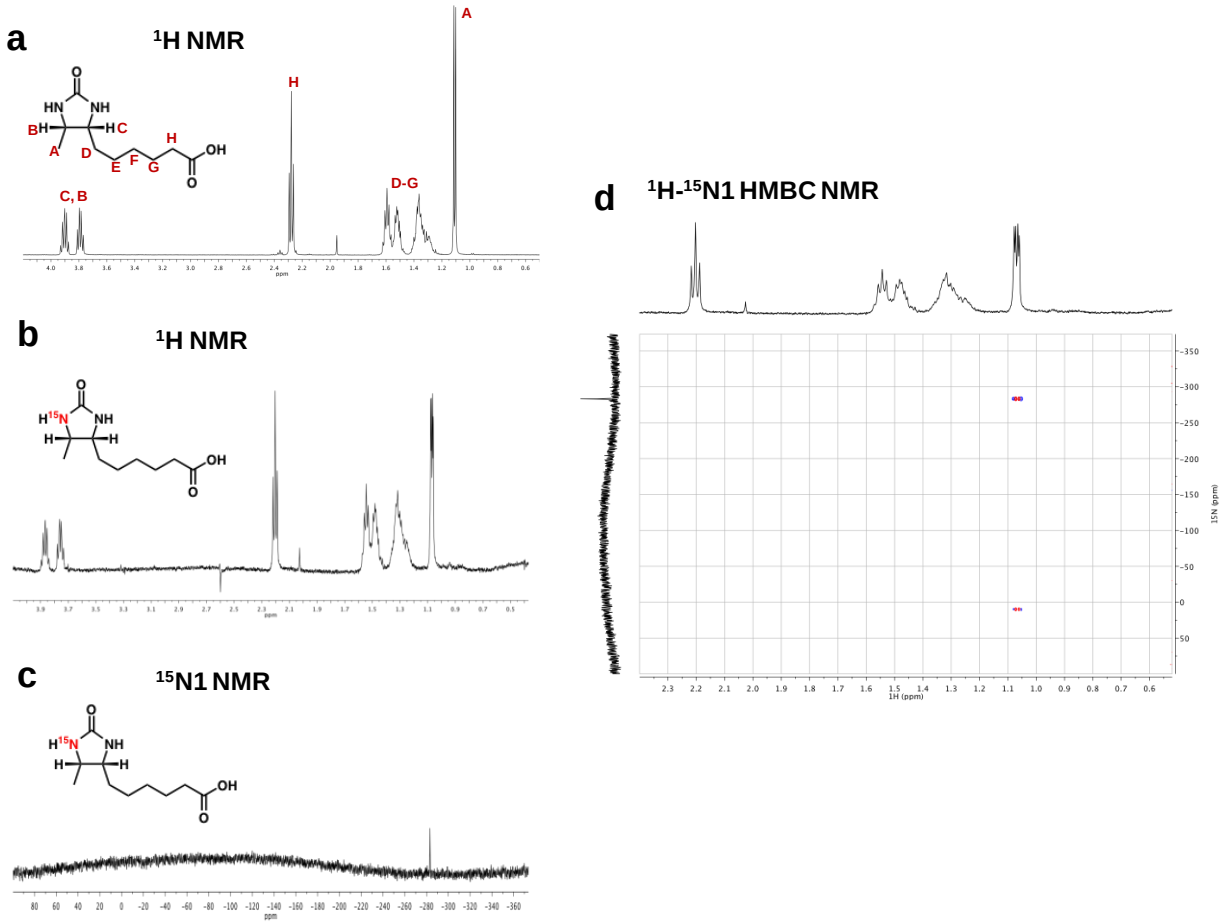

Figure S25. NMR spectra of ^{15}N1-DTB. a, ^{1}H NMR spectrum of natural abundance DTB at 500 MHz in D_2O. **b,** ^{1}H NMR spectrum of ^{15}N1-DTB at 500 MHz in D_2O. **c,** ^{15}N NMR spectrum of ^{15}N1-DTB at 500 MHz in D_2O. **d,** ^{1}H-^{15}N HMBC NMR spectra of ^{15}N1-DTB at 500 MHz in D_2O.

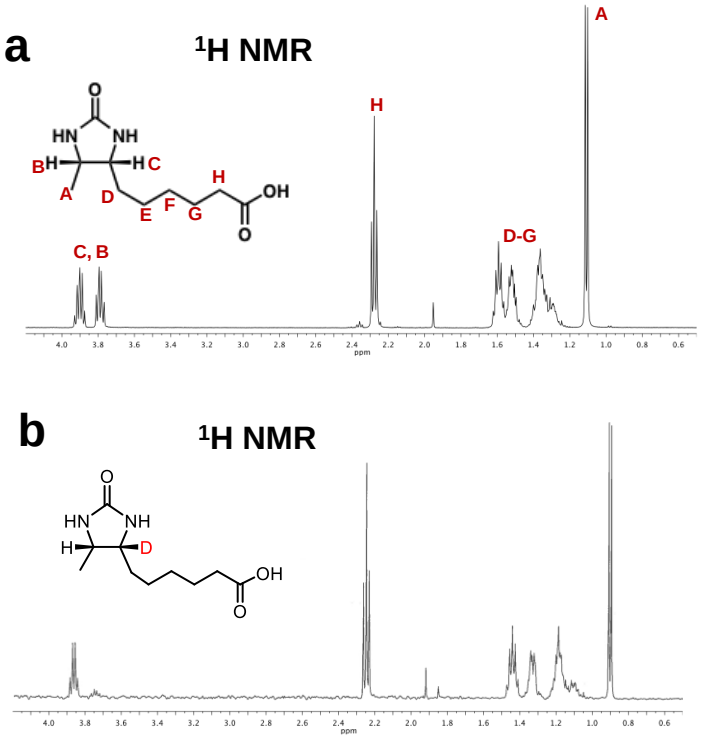

Figure S26. NMR spectra of ^{2}H7-DTB. a, ^{1}H NMR spectrum of natural abundance DTB at 500 MHz in D_2O. **b,** ^{1}H NMR spectrum of ^{2}H7-DTB at 500 MHz in D_2O.

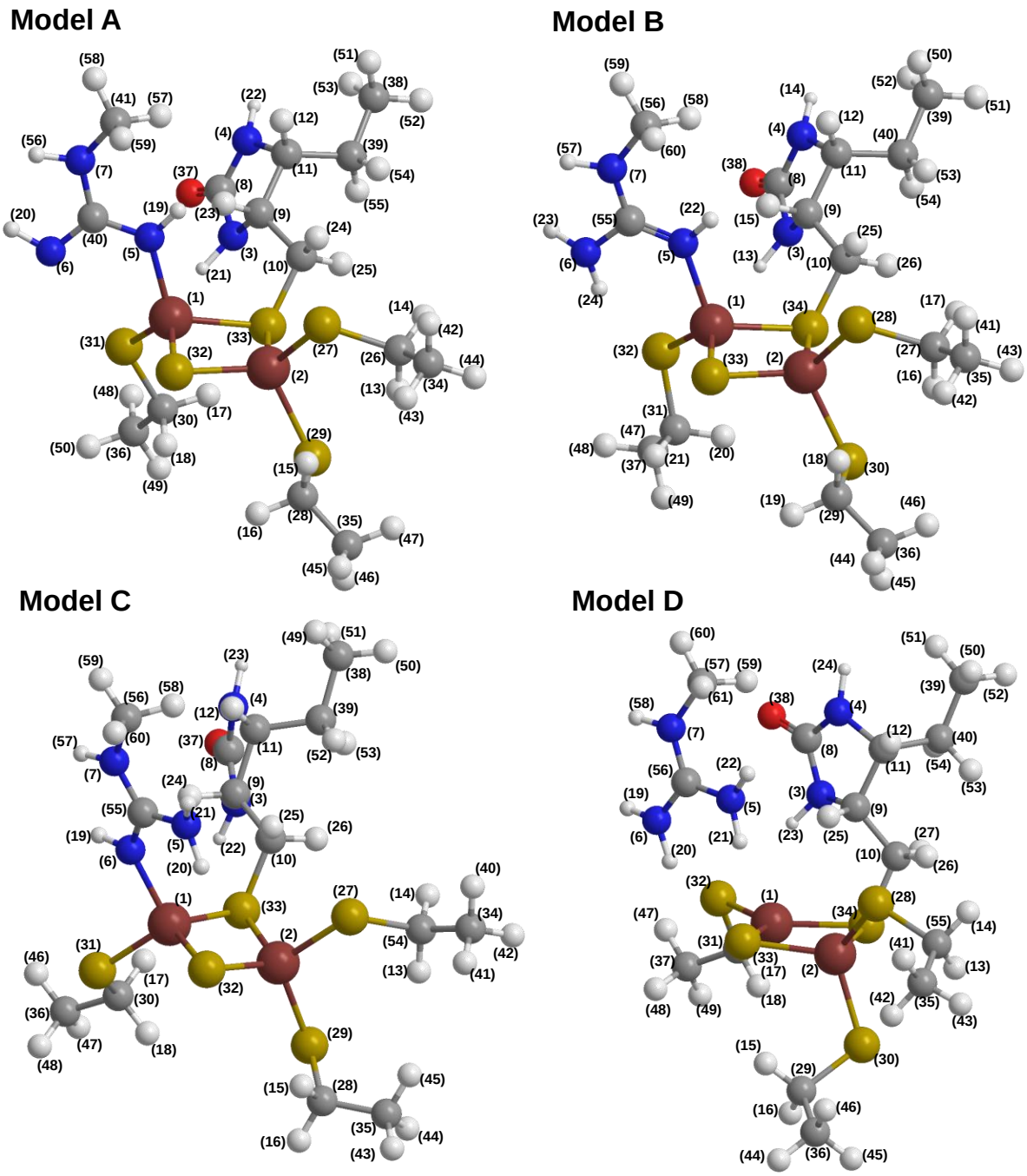

Figure S27. Ball-and-stick model of the optimized geometry of four models (A, B, C and D) of the intermediate with the atom numbers presented. The corresponding atom numbers are also given in Table S4-S7 in a separate file.

Table S1. Small ^{13}C hyperfine parameters with principle values < 1.0 MHz.

System	g_1	g_2	g_3	A(^{13}C) (MHz)			Euler angle [α, β, γ]°	a_{iso} (MHz)	T (MHz)	$r^{13}_{C\text{-}M}$ (Å)	Ref.
				A_1	A_2	A_3					
^{13}C10-DTB	1.993	1.941	1.847	0.18	0.14	0.32	[70, 125, 10]	0.21	0.05	4.89[a]	this work
Complex A-^{13}CO	2.058	1.922	1.882	0.10	0.30	0.27	[30, 30, 0]	0.22	0.07	~5[b]	17
Complex A-^{13}CN	2.058	1.922	1.882	0.15	0.30	0.28	[0, 30, 0]	0.24	0.05	~5[b]	17
Complex A ^{13}C3-Cys	2.058	1.922	1.882	1.00	0.20	1.00	[60, 35, -60]	0.73	0.27	~4[c]	17
[4Fe-4S]-^{13}C3-Cys in HydG	2.064	1.895	1.865	0.83	0.83	1.09	[0, 40, 0]	0.92	0.09	~4[c]	18
^{13}C10-Linoleic acid[c]	2.01, D = 1320 MHz[e]			-0.16	-0.16	0.35	-	0.01	0.17	4.84[f]	19
^{13}C10-Linoleic acid[d]	2.01, D = 1320 MHz[e]			-0.13	-0.13	0.29	-	0.01	0.14	5.21[f]	19
^{13}C11-Linoleic acid[c]	2.01, D = 1320 MHz[e]			-0.16	-0.16	0.35	-	0.01	0.17	4.89[f]	19
^{13}C11-Linoleic acid[d]	2.01, D = 1320 MHz[e]			-0.11	-0.11	0.22	-	0	0.11	5.65[f]	19
[4Fe-4S]-$^{13}CH_3$-SAM, PFL-AE[g]	2.01	1.88	1.87	-0.6	0.4	-0.5	[30, 30, 0]	-0.23	0.33	~4-5[h]	20
[4Fe-4S]-^{13}COO-SAM, PFL-AE[g]	2.01	1.88	1.87	1.1	-0.95	-0.82	[90, 30, 90]	-0.22	0.44	~3.3	21
[4Fe-4S]-$^{13}CH_3$-SAM, LAM[i]	2.00	1.90	1.85		~0.70		-	-	-	-	22
[4Fe-4S]-$^{13}CH_3$-anSAM, LAM[j]	2.00			-0.82	-0.82	-0.19	-	-0.61	0.21	~3.6[k]	23
[4Fe-4S]-$^{13}CH_3$-dc-SAM, *ph*Dph2[l]	2.03	1.98	1.95		~0.60		-	-	-	-	24
[4Fe-4S]-$^{13}C_\beta$OO-citrate, aconitase	2.06	1.93	1.86		~1.0		-	-	-	-	25

[a]The distance is from C10 to the nearest iron center of [2Fe-2S], based on the BS-DFT optimized geometry of model A of the paramagnetic intermediate.

[b]The distance is from the corresponding ^{13}C to the closest iron center of [4Fe-4S] cluster, based on the X-ray structure (PDB:4wcx). The distance for $^{13}CO/^{13}CN$ is obtained by assuming CO and CN^- replace the two water ligands of the dangler Fe in HydG (PDB:4wcx).

[c]Active conformer of substrate (linoleic acid) bound in Mn-soybean lipoxygenase.

[d]Inactive conformer of substrate (linoleic acid) bound in Mn-soybean lipoxygenase.

[e]Paramagnetic spin center is Mn(II) (S = 5/2) with isotropic g tensor (g = 2.01) and zero-field splitting (ZFS) D = 1320 MHz.

[f]Calculated using basic point-dipole approximation model (eq. 3) with 0.994 spin density residing on Mn(II).

[g]Pyruvate formate-lyase activating enzyme.

[h]The distance is from ^{13}C-methyl to the nearest iron center of [4Fe-4S] cluster after SAM cleavage and is calculated using the basic point-dipole approximation model (eq. 3).

[i]Lysine 2,3-aminomutase.

[j]This work investigated the hyperfine coupling of ^{13}C-methyl with spin center C5' (spin density 0.59) of the stable allylic anhydroadenosyl radical (anAdO•), after the cleavage of *S*-3',4'-anhydroadenosyl-L-methionine (anSAM).

[k]This distance is from ^{13}C-methyl to the C5' of anAdO• and is calculated using the basic point-dipole approximation model (eq. 3).

[l]$^{13}CH_3$-dc-SAM means decarboxyl SAM analogue.

Table S2 DFT-predicted hyperfine coupling tensors of the multiple nuclei in the intermediate Model A by using different dielectric constant ε.

Nucleus	Exp.		DFT (ε = 20)		DFT (ε = 4)	
	a_{iso} (MHz)	T_{dip} (MHz)	a_{iso} (MHz)	T_{dip} (MHz)	a_{iso} (MHz)	T_{dip} (MHz)
^{13}C9	2.37	[-1.07, -1.53, 2.60]	3.39	[-2.82, -0.45, 3.27]	4.19	[-2.79, -0.44, 3.23]
^{13}C8	1.43	[-0.43, -0.73, 1.16]	1.84	[-2.01, 0.32, 1.69]	1.82	[-1.99, 0.34, 1.65]
^{13}C10	0.21	[-0.03, -0.07, 0.10]	0.06	[0.18, 0.37, -0.55]	0.07	[0.18, 0.37, -0.55]
^{15}N1	-0.26	[0.12, 0.01, -0.13]	-0.58	[0.59, -0.21, -0.37]	-0.63	[0.59, -0.22, -0.37]
^{2}H7	0.05	[-0.02, -0.02, 0.04]	0.003	[0.05, 0.21, -0.26]	0.01	[0.32, 1.39, -1.71]
$^{15}N_a$	4.99	[-1.33, -0.89, 2.22]	7.15	[-1.78, 0.39, 1.39]	7.17	[-1.70, 0.34, 1.36]
$^{15}N_b$	1.26	[-0.56, 0.02, 0.54]	1.50	[-0.47, 0.11, 0.36]	1.49	[-0.48, 0.10, 0.38]

Table S3 DFT-predicted hyperfine coupling tensors of the two guanidine η-nitrogens in the three models by using different dielectric constant ε.

Model	Nucleus	DFT (ε = 20)		DFT (ε = 4)	
		a_{iso} (MHz)	T_{dip} (MHz)	a_{iso} (MHz)	T_{dip} (MHz)
A	$^{15}N_a$	7.15	[-1.78, 0.39, 1.39]	7.17	[-1.70, 0.34, 1.36]
	$^{15}N_b$	1.50	[-0.47, 0.11, 0.36]	1.49	[-0.48, 0.10, 0.38]
B	$^{15}N_a$	7.35	[-1.18, -0.44, 1.62]	7.49	[-1.11, -0.52, 1.63]
	$^{15}N_b$	0.18	[-0.20, -0.07, -0.27]	0.16	[-0.21, -0.06, -0.27]
C	$^{15}N_a$	5.86	[-1.26, -0.23, 1.49]	5.91	[0.27, 0.07, -0.34]
	$^{15}N_b$	-0.41	[0.28, 0.07, -0.35]	-0.51	[0.27, 0.07, -0.34]

References

1. Fugate, C. J.; Stich, T. A.; Kim, E. G.; Myers, W. K.; Britt, R. D.; Jarrett, J. T., 9-Mercaptodethiobiotin is generated as a ligand to the $[2Fe–2S]^{+}$ cluster during the reaction catalyzed by biotin synthase from *Escherichia coli*. *J. Am. Chem. Soc.* **2012,** *134* (22), 9042-9045.
2. Ploux, O.; Soularue, P.; Marquet, A.; Gloeckler, R.; Lemoine, Y., Investigation of the first step of biotin biosynthesis in *Bacillus sphaericus*. Purification and characterization of the pimeloyl-CoA synthase, and uptake of pimelate. *Biochem. J.* **1992,** *287* (3), 685-690.
3. Ugulava, N. B.; Gibney, B. R.; Jarrett, J. T., Biotin synthase contains two distinct iron-sulfur cluster binding sites: chemical and spectroelectrochemical analysis of iron-sulfur cluster interconversions. *Biochemistry* **2001,** *40* (28), 8343-8451.
4. Ugulava, N. B.; Surerus, K. K.; Jarrett, J. T., Evidence from Mössbauer spectroscopy for distinct $[2Fe\text{-}2S]^{2+}$ and $[4Fe\text{-}4S]^{2+}$ cluster binding sites in biotin synthase from *Escherichia coli*. *J. Am. Chem. Soc.* **2002,** *124* (31), 9050.
5. Miller, J. H., *Experiments in Molecular Genetics*. Cold Spring Harbor Press: New York, 1972.
6. Neidhardt, F. C.; Bloch, P. L.; Smith, D. F., Culture Medium for Enterobacteria. *J. Bacteriol.* **1974,** *119* (3), 736-747.
7. Baba, T.; Ara, T.; Hasegawa, M.; Takai, Y.; Okumura, Y.; Baba, M.; Datsenko, K. A.; Tomita, M.; Wanner, B. L.; Mori, H., Construction of *Escherichia coli* K-12 in-frame, single-gene knockout mutants: the Keio collection. *Mol. Syst. Biol* **2006,** *2* (1), 1-11.
8. Jarrett, J. T.; Goulding, C. W.; Fluhr, K.; Huang, S.; Matthews, R. G., Purification and assay of cobalamin-dependent methionine synthase from Escherichia coli. *Methods Enzymol.*, **1997**, 281, 196-213.
9. Abdalla, J. A. B.; Bowen, A. M.; Bell, S. G.; Wong, L. L.; Timmel, C. R.; Harmer, J., Characterisation of the paramagnetic $[2Fe\text{-}2S]^{+}$ centre in palustrisredoxin-B (PuxB) from *Rhodopseudomonas palustris* CGA009: g-matrix determination and spin coupling analysis. *Phys. Chem. Chem. Phys.* **2012,** *14* (18), 6526-6537.
10. Dikanov, S. A.; Bowman, M. K., Determination of ligand conformation in reduced [2Fe-2S] ferredoxin from cysteine β-proton hyperfine couplings. *J. Biol. Inorg. Chem.* **1998,** *3* (1), 18-29.
11. Kolling, D. R. J.; Samoilova, R. I.; Shubin, A. A.; Crofts, A. R.; Dikanov, S. A., Proton environment of reduced rieske iron−sulfur cluster probed by two-dimensional ESEEM spectroscopy. *J. Phys. Chem. A* **2009,** *113* (4), 653-667.
12. Taylor, A. M.; Stoll, S.; Britt, R. D.; Jarrett, J. T., Reduction of the [2Fe–2S] cluster accompanies formation of the intermediate 9-Mercaptodethiobiotin in *Escherichia coli* biotin synthase. *Biochemistry* **2011,** *50* (37), 7953-7963.
13. Jameson, G. N. L.; Cosper, M. M.; Hernández, H. L.; Johnson, M. K.; Huynh, B. H., Role of the [2Fe−2S] cluster in recombinant *Escherichia coli* biotin synthase. *Biochemistry* **2004,** *43* (7), 2022-2031.
14. Hoffman, B. M., Electron nuclear double resonance (ENDOR) of metalloenzymes. *Acc. Chem. Res.* **1991,** *24* (6), 164-170.
15. Randall, D. W.; Gelasco, A.; Caudle, M. T.; Pecoraro, V. L.; Britt, R. D., ESE-ENDOR and ESEEM characterization of water and methanol ligation to a dinuclear Mn(III)Mn(IV) complex. *J. Am. Chem. Soc.* **1997,** *119* (19), 4481-4491.
16. Berkovitch, F.; Nicolet, Y.; Wan, J. T.; Jarrett, J. T.; Drennan, C. L., Crystal structure of biotin synthase, an *S*-adenosylmethionine-dependent radical enzyme. *Science* **2004,** *303* (5654), 76-79.
17. Rao, G.; Tao, L.; Suess, D. L. M.; Britt, R. D., A [4Fe–4S]-Fe(CO)(CN)-l-cysteine intermediate is the first organometallic precursor in [FeFe] hydrogenase H-cluster bioassembly. *Nature Chemistry* **2018,** *10* (5), 555-560.
18. Suess, D. L. M.; Bürstel, I.; De La Paz, L.; Kuchenreuther, J. M.; Pham, C. C.; Cramer, S. P.; Swartz, J. R.; Britt, R. D., Cysteine as a ligand platform in the biosynthesis of the FeFe hydrogenase H cluster. *Proc. Natl. Acad. Sci. USA* **2015,** *112* (37), 11455-11460.

19. Horitani, M.; Offenbacher, A. R.; Carr, C. A. M.; Yu, T.; Hoeke, V.; Cutsail, G. E.; Hammes-Schiffer, S.; Klinman, J. P.; Hoffman, B. M., ^{13}C ENDOR spectroscopy of Lipoxygenase–substrate complexes reveals the structural basis for C–H activation by tunneling. *J. Am. Chem. Soc.* **2017,** *139* (5), 1984-1997.
20. Walsby, C. J.; Hong, W.; Broderick, W. E.; Cheek, J.; Ortillo, D.; Broderick, J. B.; Hoffman, B. M., Electron-nuclear double resonance spectroscopic evidence that *S*-Adenosylmethionine binds in contact with the catalytically active [4Fe−4S]$^{+}$ cluster of pyruvate formate-lyase activating enzyme. *J. Am. Chem. Soc.* **2002,** *124* (12), 3143-3151.
21. Walsby, C. J.; Ortillo, D.; Broderick, W. E.; Broderick, J. B.; Hoffman, B. M., An anchoring role for FeS clusters: chelation of the amino acid moiety of *S*-Adenosylmethionine to the unique iron site of the [4Fe−4S] cluster of pyruvate formate-lyase activating enzyme. *J. Am. Chem. Soc.* **2002,** *124* (38), 11270-11271.
22. Chen, D.; Walsby, C.; Hoffman, B. M.; Frey, P. A., Coordination and mechanism of reversible cleavage of *S*-Adenosylmethionine by the [4Fe-4S] center in Lysine 2,3-Aminomutase. *J. Am. Chem. Soc.* **2003,** *125* (39), 11788-11789.
23. Horitani, M.; Byer, A. S.; Shisler, K. A.; Chandra, T.; Broderick, J. B.; Hoffman, B. M., Why Nature uses radical SAM enzymes so widely: electron nuclear double resonance studies of Lysine 2,3-Aminomutase show the 5′ -dAdo• "free radical" is never free. *J. Am. Chem. Soc.* **2015,** *137* (22), 7111-7121.
24. Dong, M.; Horitani, M.; Dzikovski, B.; Freed, J. H.; Ealick, S. E.; Hoffman, B. M.; Lin, H., Substrate-dependent cleavage site selection by unconventional radical *S*-Adenosylmethionine enzymes in diphthamide biosynthesis. *J. Am. Chem. Soc.* **2017,** *139* (16), 5680-5683.
25. Kennedy, M. C.; Werst, M.; Telser, J.; Emptage, M. H.; Beinert, H.; Hoffman, B. M., Mode of substrate carboxyl binding to the [4Fe-4S]$^{+}$ cluster of reduced aconitase as studied by ^{17}O and ^{13}C electron-nuclear double resonance spectroscopy. *Proc. Natl. Acad. Sci. USA* **1987,** *84* (24), 8854-8858.